

¹ Study of the multi-strange resonance $\Xi(1530)^0$ production
² with ALICE at the LHC energies

³ Jihye Song

4 Contents

5	List of Figures	4
6	List of Tables	6
7	1 The physics of relativistic heavy-ion collisions	7
8	1.1 Standard model	7
9	1.2 Quantum Chromo-Dynamics	7
10	1.3 Heavy Ion Collisions	7
11	2 Production of resonance with strangeness	7
12	2.1 Resonance with strangeness	7
13	3 Theoretical models	7
14	3.1 Thermal statistical model	7
15	3.1.1 Calculations	9
16	3.1.2 Results	9
17	3.1.3 Comparison with data	11
18	3.2 UrQMD	11
19	4 A Large Ion Collider Experiment at the LHC	11
20	4.1 The Large Hadron Collider	12
21	4.2 The ALICE project	12
22	4.2.1 ALICE detector	12
23	4.2.2 Data Acquisition (DAQ) and trigger system	12
24	4.2.3 ALICE offline software frame work	12
25	5 Measurement of $\Xi(1530)^0$ production in p-Pb and Pb-Pb	12
26	5.1 $\Xi(1530)^0$ -reconstruction	13
27	5.1.1 Data sample and event selection	13
28	5.1.2 Track and topological selection	16
29	5.1.3 Particle identification	19
30	5.1.4 Signal extraction	22
31	5.2 Efficiency correction	31
32	5.3 Corrected p_T -spectra	34
33	5.4 Systematic uncertainties	36
34	5.5 $\Xi(1530)^0$ transverse momentum spectra	41
35	6 Results	46
36	6.1 dN/dy and $\langle p_T \rangle$	46
37	6.2 Particle yield ratios	46

38	6.2.1	Comparison with other resonances	46
39	6.2.2	Comparison with models	46
40	References		46

⁴¹ **List of Figures**

42	1	Ratio of baryonic and mesonic resonances over their stable partner as a function of temperature.	10
44	2	Ratio of resonances over their stable partner as a function of $\sqrt(s)$	11
45	3	Vertex-z coordinate distribution of the accepted events in p–Pb collision(Left) and in Pb–Pb collisions(Right). The red dashed line indicates vertex cut .	14
47	4	Multiplicity distribution of accepted events in p–Pb collision in percentile. The each color and labels define the four intervals in which the analysis is performed.	15
50	5	Centrality distribution of three different trigger classes.	16
51	6	Sketch of the decay modes for Ξ^*0 and depiction of the track and topological selection criteria.	18
53	7	TPC dE/dx as function of transverse momentum for total (top) and selected first emitted π in 3σ (bottom)	19
55	8	TPC dE/dx as function of transverse momentum for total (top) and selected second emitted π in 3σ (bottom)	19
57	9	TPC dE/dx as function of transverse momentum for total (top) and selected last emitted π in 3σ (bottom)	20
59	10	TPC dE/dx as function of transverse momentum for total (top) and selected proton in 3σ (bottom)	20
61	11	TPC dE/dx as function of transverse momentum for total (top) and selected first emitted π in 3σ (bottom)	20
63	12	TPC dE/dx as function of transverse momentum for total (top) and selected second emitted π in 3σ (bottom)	21
65	13	TPC dE/dx as function of transverse momentum for total (top) and selected last emitted π in 3σ (bottom)	21
67	14	TPC dE/dx as function of transverse momentum for total (top) and selected proton in 3σ (bottom)	22
69	15	The $\Xi^\mp\pi^\pm$ invariant mass distribution (Same-event pairs) in $1.8 < p_T < 2.2 \text{ GeV}/c$ and for the multiplicity class 20-40%. The background shape, using pairs from different events (Mixed-event background), is normalised to the counts in $1.49 < M_{\Xi\pi} < 1.51 \text{ GeV}/c^2$ and $1.56 < M_{\Xi\pi} < 1.58 \text{ GeV}/c^2$	23
73	16	The $\Xi^\mp\pi^\pm$ invariant mass distribution (Same-event pairs) in $3.0 < p_T < 3.5 \text{ GeV}/c$ and for the centrality class 0-10%. The background shape, using pairs from different events (Mixed-event background), is normalised to the counts in $1.49 < M_{\Xi\pi} < 1.51 \text{ GeV}/c^2$ and $1.56 < M_{\Xi\pi} < 1.58 \text{ GeV}/c^2$	24
77	17	The invariant mass distribution after subtraction of the mixed-event background in p–Pb collisions. The solid curve represents the combined fit, while the dashed line describes the residual background.	25

80	18	The invariant mass distribution after subtraction of the mixed-event background in Pb–Pb collisions. The solid curve represents the combined fit, while the dashed line describes the residual background.	26
81	19	σ fit parameters as a function of p_{T} in MB in p–Pb collisions (top) and in Pb–Pb collisions (bottom).	28
82	20	$\Xi(1530)^0$ -mass obtained from fit of the Voigtian peak as a function of p_{T} in each multiplicity classes in p–Pb collisions (top) and the different centrality classes in Pb–Pb (bottom).	29
83	21	$\Xi(1530)^0$ -raw spectra obtained from fit of the Voigtian peak and a polynomial residual background for different multiplicities in p–Pb collisions (top) and Pb–Pb collisions (bottom). Only the statistical error is reported.	30
84	22	$\Xi(1530)^0$ -raw spectra obtained from fit of the Voigtian peak and a polynomial residual background for different multiplicities. Only the statistical error is reported.	31
85	23	Real corrected $\Xi(1530)^0$ spectrum (black) for the minimum bias with Levy fit (black curve). Also shown are the unweighted generated (blue) and reconstructed (red) $\Xi(1530)^0$ spectra.	32
86	24	Efficiency as a function of p_{T} in minimum bias events in p–Pb collisions.	33
87	25	Efficiency as a function of p_{T} in different centrality classes in Pb–Pb collisions	34
88	26	Corrected p_{T} -spectra of $\Xi(1530)^0$ in NSD and different multiplicity classes in p–Pb collisions.	35
89	27	Corrected p_{T} -spectra of $\Xi(1530)^0$ in different centrality classes in Pb–Pb collisions.	35
90	28	Summary of the contributions to the systematic uncertainty in minimum bias events in p–Pb collisions. The dashed black line is the sum in quadrature of all the contributions.	39
91	29	Systematic uncertainties for each multiplicity classes in p–Pb collisions.	39
92	30	Summary of the contributions to the systematic uncertainty in minimum bias events in Pb–Pb collisions. The dashed black line is the sum in quadrature of all the contributions.	40
93	31	Systematic uncertainties for each multiplicity classes.	40
94	32	Corrected yields as function of p_{T} in NSD events and multiplicity dependent event classes in p–Pb collision system. Statistical uncertainties are presented as bar and systematical uncertainties are plotted as boxes.	42
95	33	Corrected yields as function of p_{T} in different centrality classes in Pb–Pb collision system. Statistical uncertainties are presented as bar and systematical uncertainties are plotted as boxes.	43
96	34	Integrated.	44
97	35	Integrated.	45

¹¹⁹ **List of Tables**

120	1	Parameters used in the thermal-model calculations.	8
121	2	Properties of particles used in the ratio calculations.	9
122	3	Difference of mass (ΔM), baryon number (ΔB), strangeness (ΔS) and charge (ΔQ) of the ratios. The values of the slopes needs to be checked!!!! .	11
123	4	Number of accepted and analyzed events per multiplicity/centrality interval	16
124	5	Track selections common to all decay daughters and primary track selections applied to the charged pions from decays of Ξ^{*0}	17
125	6	Topological and track selection criteria.	17
126	7	Summary of the systematic uncertainties on the differential yield, $d^2N/(dp_T dy)$. Minimum and maximum values in all p_T intervals and multiplicity classes in p–Pb, centrality classes in Pb–Pb are shown for each source.	41
127			
128			
129			
130			

131 **1 The physics of relativistic heavy-ion collisions**

132 This test for references [1]

133 **1.1 Standard model**

134 **1.2 Quantum Chromo-Dynamics**

135 **1.3 Heavy Ion Collisions**

136 **2 Production of resonance with strangeness**

137 **2.1 Resonance with strangeness**

138 **3 Theoretical models**

139 **3.1 Thermal statistical model**

140 The statistical-thermal model has proved extremely successful in applications to relativistic
141 collisions of both heavy ions and elementary particles. In light of this success, THERMUS,
142 a thermal model analysis package, has been developed for incorporation into the object-
143 oriented ROOT framework [2].

144 There are three types of statistical-thermal models in explaining data in high energy nu-
145 clear physics and THERMUS treats the system quantum numbers B (baryon number), S
146 (strangeness) and Q (charge) within three distinct formalisms:

148 1. **Grand-Canonical Ensemble:** Because the hot dense matter produced in nucleus-
149 nucleus collisions is large enough, this ensemble is the most widely used in applications
150 to heavy-ion collisions, in which the quantum numbers are conserved on average.

151 2. **Fully-Canonical Ensemble:** In which B, S and Q are each exactly conserved and
152 this ensemble used in high-energy elementary collisions such as pp, p \bar{p} and e $^-$ e $^+$
153 collisions.

154 3. **Strangeness-Canonical Ensemble:** In small systems or at low temperatures, a
155 canonical treatment leads to a suppression of hadrons carrying non-zero quantum
156 numbers, since these particles have to be created in pairs and the resulting low
157 production of strange particles requires a canonical treatment of strangeness.

158 In order to calculate the thermal properties of a system, one starts with an evaluation
159 of its partition function. The form of the partition function obviously depends on the
160 choice of ensemble. In the present analysis the strangeness-canonical ensemble used and
161 the statistical-thermal model requires six parameters as input: the chemical freeze-out

162 temperature T , baryon and charge chemical potentials μ_B and μ_Q respectively, canonical
163 or correlation radius, R_C ; the radius inside which strangeness is exactly conserved and the
164 fireball radius R . An additional strangeness saturation factor γ_S has been used as indicator
165 of a possible departure from equilibrium and $\gamma_S = 1.0$ corresponds to complete strangeness
166 equilibration.

167 The volume dependence cancels out when studying the particle ratios as well as strangeness
168 canonical equivalent to grand canonical formalism if $\Delta S = 0$ in the ratios and γ_S also can-
169 cels out. Parameters used in the analysis listed in Table 1. The μ_B parameter taken from
170 the Ref. [3].

Table 1: Parameters used in the thermal-model calculations.

Parameter	Value
T (MeV)	varied (see text)
μ_B (MeV)	$9.2 \times 10^{-2}????$
μ_Q (MeV)	0.0
γ_S	1.0

172 **3.1.1 Calculations**

173 *Concept:*

174 In order to calculate the particle ratios within strangeness canonical formalism of THER-
 175 MUS, temperature varied between 60 MeV to 180 MeV and particle yields extracted for
 176 each temperature value and then primary particle ratios calculated for each case.

177

178 *Feed-Down Correction:*

179 Since the particle yields measured by the detectors in collision experiments include feed-
 180 down from heavier hadrons and hadronic resonances, the primordial hadrons are allowed to
 181 decay to particles considered stable by the experiment before model predictions are com-
 182 compared with experimental data. In the analysis only Λ particles counted as stable (do not
 183 allowed to decay) so there is no feed-down contribution from these particles to the other
 184 ratios.

185

186

187 Properties of studied particles and their particle ratios listed in Table 2 and Table 3,
 188 respectively.

Table 2: Properties of particles used in the ratio calculations.

Particle	Δ^{++}	p	K^{*0}	K^0	K^+	Λ^*	Λ	Σ^{*+}	Σ^+	Σ^0
Mass (MeV/c^2)	1232	938.27	895.92	497.61	493.67	1519.5	1115.68	1382.8	1189.37	1192.6
Width (MeV/c^2)	120	–	50.7	–	–	15.6	–	37.6	–	–
$c\tau$ (fm)	1.6	–	3.9	–	–	12.6	–	5.51	–	–
Ang. Momentum (J)	3/2	1/2	1	1	0	3/2	1/2	3/2	1/2	1/2
Isospin (I)	3/2	1/2	1/2	1/2	1/2	0	0	1	1	1
Parity (P)	+1	+1	-1	-1	0	-1	+1	+1	+1	+1
Strangeness (S)	0	0	1	1	1	-1	-1	-1	-1	-1
Baryon Number (B)	1	1	0	0	0	1	1	1	1	1
Decay Channel	$p\pi^+$	–	π^-	–	$\mu^+\nu_\mu$	pK^-	$p\pi^-$	$\Lambda\pi^+$	$p\pi^0$	$\Lambda\gamma$
Branching Ratio (%)	~ 100	–	~ 66.7	–	~ 63.54	~ 45	~ 63.9	~ 87	~ 51.6	~ 100
Q-Value(MeV/c^2)	154.16	–	262.68	–	–	87.55	37.84	127.55	111.53	76.96

189

190

191 **3.1.2 Results**

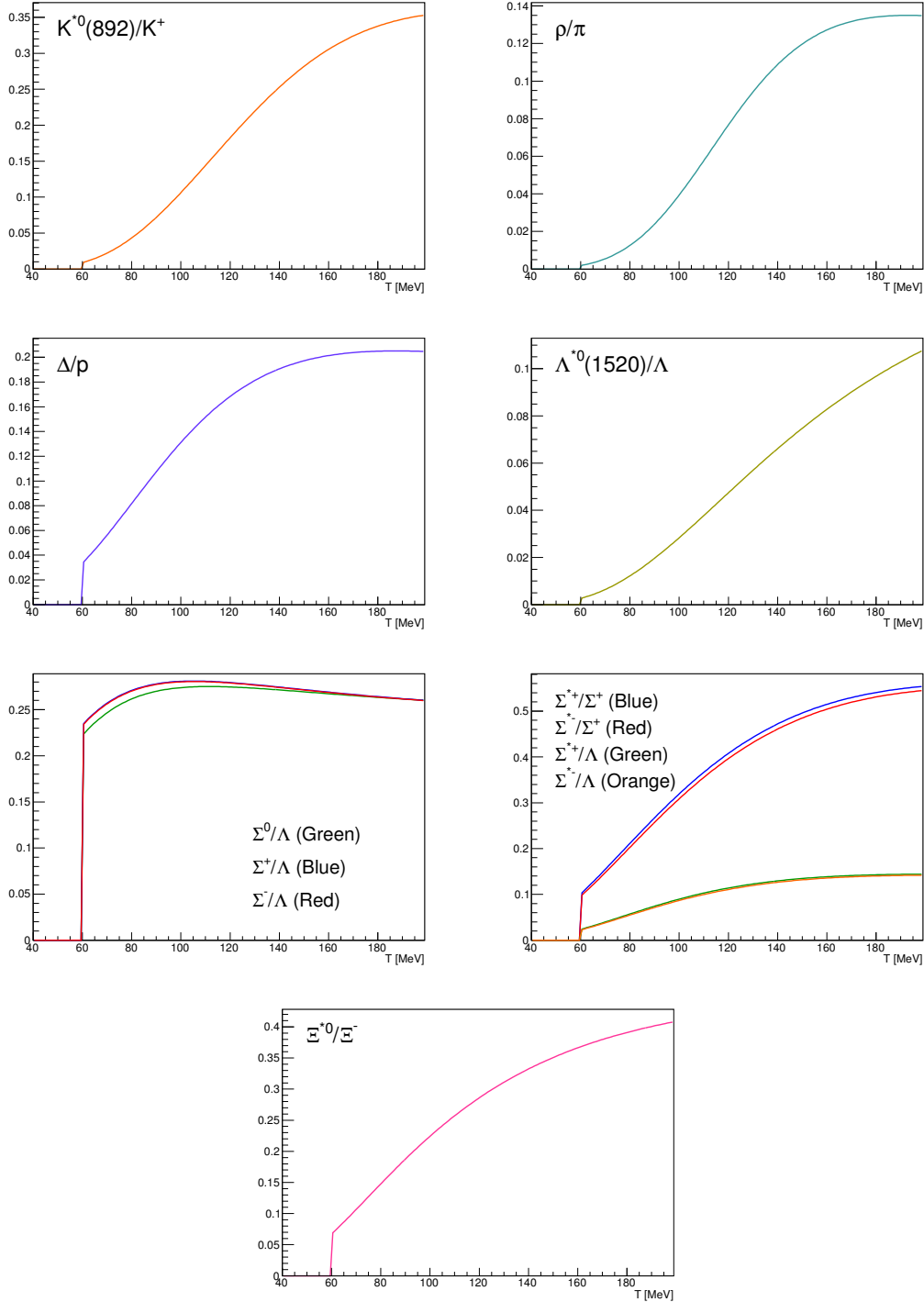


Figure 1: Ratio of baryonic and mesonic resonances over their stable partner as a function of temperature.

Table 3: Difference of mass (ΔM), baryon number (ΔB), strangeness (ΔS) and charge (ΔQ) of the ratios. The values of the slopes needs to be checked!!!!

Particle	Δ^{++}/p	K^*/K^+	Λ^*/Λ	Σ^{*+}/Λ	Σ^{*+}/Σ^0	Σ^0/Λ	Σ^{*+}/Σ^+	Ξ^{*0}/Ξ^-
ΔM (MeV/ c^2)	293.8	402.25	403.82	267.12	190.16	76.96	193.43	210.49
ΔB	0	0	0	0	0	0	0	0
ΔS	0	0	0	0	0	0	0	0
ΔQ	+1	-1	0	+1	0	+1	0	-1
Slope (%) per MeV ????????	0.19	0.76	0.98	0.25	-	-0.08	0.37	0.42

192 3.1.3 Comparison with data

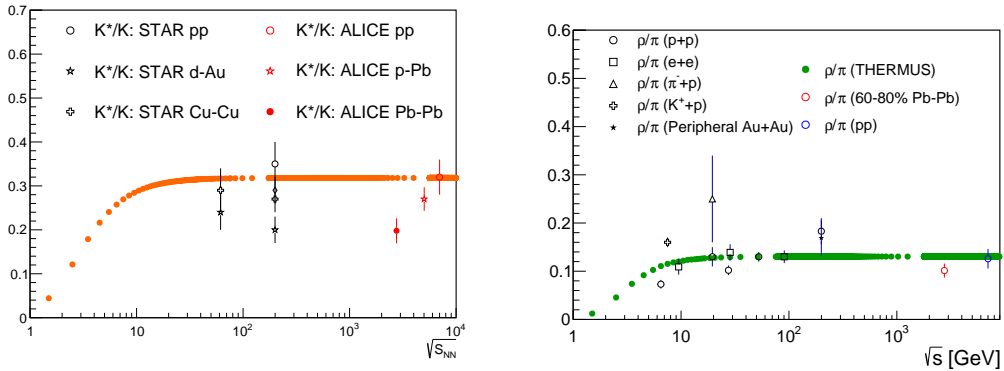


Figure 2: Ratio of resonances over their stable partner as a function of $\sqrt{(s)}$.

193 3.2 UrQMD

194 4 A Large Ion Collider Experiment at the LHC

195 ALICE (A Large Ion Collider Experiment) has been collecting data during the whole first
 196 phase of the Large Hadron Collider operations, from its startup on the 23 November 2009
 197 to the beginning of the first long technical shutdown in February 2013. During the first
 198 three years of operations LHC provided pp collisions at 0.9, 2.76, 7 and 8 TeV, Pb?Pb
 199 collisions at 2.76A TeV and finally p?Pb collisions at 5.02 TeV. The first section of this
 200 chapter focuses on the LHC performance during this phase and includes details on the
 201 accelerator parameters that allow the LHC to perform as a lead ion collider. A detailed
 202 description of the ALICE detector follows in the section 2.2. ALICE has been designed and

203 optimized to study the high particle-multiplicity environment of ultra-relativistic heavy-ion
204 collisions and its tracking and particle identification performance in Pb-Pb collisions are
205 discussed. The attention is drawn in particular on the central barrel detectors. Section
206 2.3 de- scribes the ALICE Data Acquisition (DAQ) system, that also embeds tools for the
207 online Data Quality Monitoring (DQM). The final part of the chapter is dedicated to the
208 offline computing and reconstruction system based on the GRID framework.

209 **4.1 The Large Hadron Collider**

210 The Large Hadron Collider (LHC) [57], [58] is a two-ring-superconducting hadron accel-
211 erator and collider installed in the 26.7 Km tunnel that hosted the LEP ma- chine and it
212 completes the CERN accelerator complex together with the PS and SPS, among the others
213 shown in fig. 2.1. Four main experiments are located in four different interaction points
214 along its circumference. ATLAS and CMS, the biggest ones, are multi-purpose detectors
215 built to discover the Higgs boson and hints of new physics beyond the Standard Model.
216 LHCb is dedicated to the physics of the flavour, focusing on the study CP-violation using B
217 meson decay channels. The phenomena that these three experiments aim to observe have
218 production cross sec- tion of the order of a hundred of pb or lower, therefore a large number
219 of collision events is required to the machine in order to fulfill the LHC pp physics program.
220 ALICE, on the contrary, is dedicated to the physics of Quark Gluon Plasma through the
221 observation of high-energy heavy-ion collisions, although a shorter physics pro- gram with
222 pp collisions has been carried out.

223 **4.2 The ALICE project**

224 **4.2.1 ALICE detector**

225 **4.2.2 Data Acquisition (DAQ) and trigger system**

226 **4.2.3 ALICE offline software frame work**

227 **5 Measurement of $\Xi(1530)^0$ production in p–Pb and Pb–Pb**

228 The measurement of resonance production in p–Pb collisions helps to disentangle cold
229 nuclear matter effects from genuine hot medium effects and contribute to the study of
230 the system size dependence of re-scattering in the hadronic phase. And the measurement
231 in ultra-relativistic heavy-ion collisions such as Pb–Pb collisions, provide information on
232 the properties of hadronic medium and different stage of its evolution. In order to study
233 the particle production mechanism in the hadronic phase between the chemical and ki-
234 netic freeze-out, the $\Xi(1530)^0$ resonance production at mid-rapidity($-0.5 < y_{\text{CMS}} < 0$) is
235 measured in p–Pb collisions $\sqrt{s_{\text{NN}}} = 5.02$ TeV and in Pb–Pb collisions with $|y| < 0.5$ at
236 $\sqrt{s_{\text{NN}}} = 2.76$ TeV with the ALICE experiment, via the reconstruction of its hadronic decay
237 into $\Xi\pi$.

238 **5.1 $\Xi(1530)^0$ -reconstruction**

239 The Ξ^{*0} production in p–Pb and Pb–Pb collisions at mid-rapidity has been studied in dif-
240 ferent multiplicity classes, from very central to peripheral collisions. The analysis strategy
241 is based on the invariant mass study of the reconstructed pairs (referred to as the candi-
242 dates) whose provenance could be the decay of a Ξ^{*0} baryon into charged particles. The
243 decay products (also called daughters in the text) are identified as oppositely charged Ξ and
244 π among the tracks reconstructed in the central barrel. The event selection, track selec-
245 tion and the particle identification strategy is described. The raw signal yield is extracted
246 by fitting the background-subtracted invariant mass distribution in several transverse mo-
247 mentum intervals. In order to extract the p_T -dependent cross section, these yields are
248 corrected for efficiency. The p_T -dependent correction due to the detector acceptance and
249 reconstruction efficiency, $(\text{Acc} \times \epsilon_{rec})(pt)$, is computed from a Monte Carlo simulation.
250 The absolute normalisation is then performed, by dividing for the number of the events in
251 each multiplicity and centrality classes.

252 **5.1.1 Data sample and event selection**

253 A description of the ALICE detector and of its performance during the LHC Run 1 (2010–
254 2013) can be found in [4, 5]. The data sample in the analysis from Pb–Pb collisions with
255 energy of $\sqrt{s_{\text{NN}}}=2.76$ obtained during 2011 and the sample of p–Pb run at $\sqrt{s_{\text{NN}}}=5.02$
256 TeV was recorded in 2013.

257 Due to the asymmetric energies of the proton (4 TeV) and lead ion (1.57 A TeV) beams,
258 the centre-of-mass system in the nucleon-nucleon frame is shifted in rapidity by $\Delta y_{\text{NN}} =$
259 0.465 towards the direction of the proton beam with respect to the laboratory frame of
260 the ALICE detector [6]. For the analysed p–Pb data set, the direction of the proton beam
261 was towards the ALICE muon spectrometer, the so-called “C” side, standing for negative
262 rapidities; conversely, the Pb beam circulated towards positive rapidities, labelled as “A”
263 side in the following. The analysis in this paper was carried out at midrapidity, in the
264 rapidity window $-0.5 < y_{\text{CMS}} < 0$.

265 The minimum-bias trigger during the p–Pb run was configured to select events by
266 requiring a logical OR of signals in V0A and V0C [5], two arrays of 32 scintillator detectors
267 covering the full azimuthal angle in the pseudo-rapidity regions $2.8 < \eta_{\text{lab}} < 5.1$ and
268 $-3.7 < \eta_{\text{lab}} < -1.7$, respectively [7]. In the data analysis it was required to have a
269 coincidence of signals in both V0A and V0C in order to reduce the contamination from
270 single-diffractive and electromagnetic interactions. Out of this sample in p–Pb collision
271 events about 109.3 million events, 93.9 million events satisfy the following selection criteria
272 and have been actually used for the analysis.

273 The Pb–Pb collisions data sample was selected by online centrality trigger requiring
274 a signal in the forward V0 detectors[8] to record enhanced data in central collision. The
275 data consists of 24.8 million events in most central collisions (0-10%), 21.8 million events in
276 semi-central collisions (10-50%) and 3.5 million events with minimum-bas trigger (0-90%).

277 Among 49.6 million events in total, 43.0 million events have been analyzed as passed the
 278 criteria below.

- 279 • Events with z-coordinate of primary vertex (V_z) falling within ± 10 cm from the
 280 interaction point
- 281 • Rejection of pile-up event
- 282 • Requiring primary tracks to have at least one hit in one of the two innermost layers
 283 of the ITS (silicon pixel detector, SPD)
- 284 • p–Pb: multiplicity ranges in percentile (V0A): 0-20%, 20-40%, 40-60%, 60-100% and
 285 MB(0-100%)
- 286 • Pb–Pb: centrality classes (V0A and V0C): 0-10%, 10-40%, 40-80% and MB (0-80%)

287 The distribution of the vertex z position of the accepted events in p–Pb collision is
 288 reported on left panel in Figure 3 and corresponding figure but obtained from Pb–Pb
 289 collisions is shown on right panel in Figure. 3. Events with $|V_z| < 10$ cm have been used
 290 to ensure a uniform acceptance in the central pseudo-rapidity region, $|\eta| < 0.8$, where the
 291 analysis is performed. This cut reduces the total number of events to 97.5 million events,
 292 that is the $\sim 89.2\%$ of the initial sample in p–Pb collisions and 43.04 million events which
 293 is $\sim 86.8\%$ of the initial sample in Pb–Pb collisions are survived.

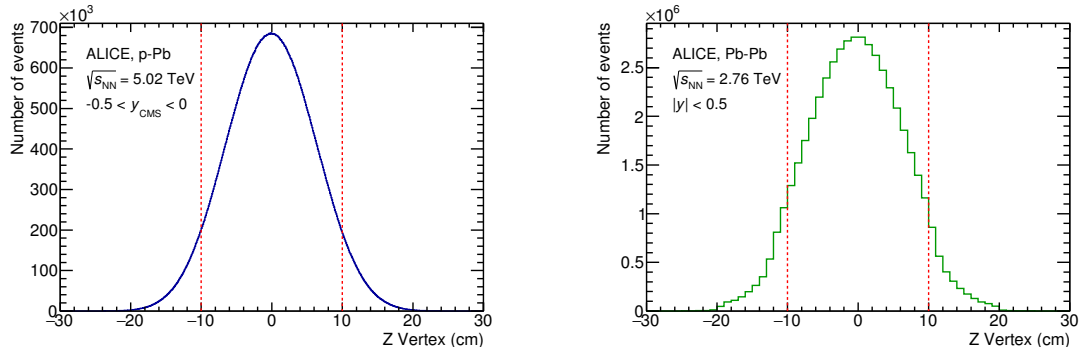


Figure 3: Vertex-z coordinate distribution of the accepted events in p–Pb collision(Left) and in Pb–Pb collisions(Right). The red dashed line indicates vertex cut

294 Fig. 4 shows the multiplicity distribution of the accepted events in p–Pb collision
 295 divided in bins of percentile. The each color on the histogram indicate the multiplicity
 296 ranges used in this analysis. Corresponding events for each multiplicity range are in Table
 297 4.

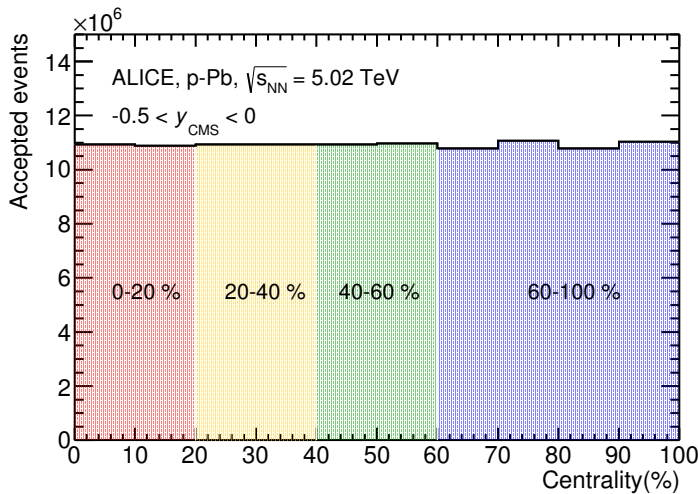


Figure 4: Multiplicity distribution of accepted events in p–Pb collision in percentile. The each color and labels define the four intervals in which the analysis in performed.

298 The distribution of centrality in each trigger used to select the events in Pb–Pb collision
 299 is shown in Fig. 5 and the reason why the centrality has step structure is that there are
 300 three different trigger classes classified by the amplitude threshold on VZERO detector.
 301 Because the distribution of events as function of centrality is not a flat, this may lead to
 302 additional bias, in particular when one needs to combine the results from different triggers.
 303 For example, events from 40-80% centrality bin have bias with high statistics in 40-60%. In
 304 order to avoid this effect, we have applied a flattening procedure to have flat distribution
 305 of events as function of centrality. A brief explanation of the method is below :

- 306 1. Histograms are obtained for the effective mass distribution in 1% centrality bins and
 307 for the centrality distribution
 308 2. The effective mass distributions are scaled in each 1% centrality bin by a factor:
 309 Factor = Nevent in 20-40% / 20 / Nevent in current 1% bin
 310 3. Each bin in the centrality distribution is scaled using the factor described above
 311 4. Histograms are added for centrality bins of interest: 0-10%, 10-40%, 40-80%, 0-80%

312 The resulting number of events in each centrality classes is summarized in Table 4.

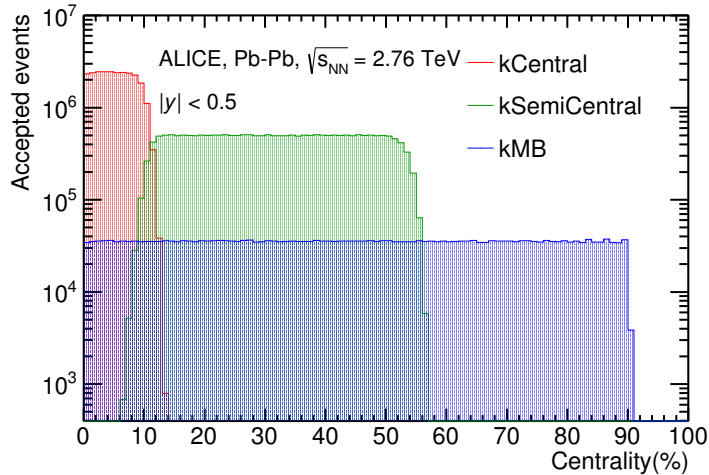


Figure 5: Centrality distribution of three different trigger classes.

p-Pb	0-20%	21.82×10^6
	20-40%	21.86×10^6
	40-60%	21.91×10^6
	60-100%	43.68×10^6
Pb-Pb	0-10%	5.58×10^6
	10-40%	16.73×10^6
	40-80%	22.31×10^6

Table 4: Number of accepted and analyzed events per multiplicity/centrality interval

313 5.1.2 Track and topological selection

314 In comparison with the Ξ^{*0} analysis carried out in pp collisions at $\sqrt{s} = 7$ TeV [9], track
 315 and topological selections were revised and adapted to the p-Pb dataset. Pions from strong
 316 decays of Ξ^{*0} were selected according to the criteria for primary tracks. As summarized
 317 in Table 5, all charged tracks were selected with $p_T > 0.15$ GeV/c and $|\eta_{\text{lab}}| < 0.8$, as
 318 described in Ref. [5]. The primary tracks were chosen with the Distance of Closest Approach
 319 (DCA) to PV of less than 2 cm along the longitudinal direction (DCA_z) and lower than $7\sigma_r$
 320 in the transverse plane (DCA_r), where σ_r is the resolution of DCA_r . The σ_r is strongly
 321 p_T -dependent and lower than 100 μm for $p_T > 0.5$ GeV/c [5]. To ensure a good track
 322 reconstruction quality, candidate tracks were required to have at least one hit in one of the
 323 two innermost layers (SPD) of the ITS and to have at least 70 reconstructed points in the

324 Time Projection Chamber (TPC), out of a maximum of 159. The Particle IDentification
 325 (PID) criteria for all decay daughters are based on the requirement that the specific energy
 326 loss (dE/dx) is measured in the TPC within three standard deviations (σ_{TPC}) from the
 expected value (dE/dx_{exp}), computed using a Bethe-Bloch parametrization [5].

Common track selections	$ \eta_{\text{lab}} $	< 0.8
	p_T	$> 0.15 \text{ GeV}/c$
	PID $ (\text{d}E/\text{d}x) - (\text{d}E/\text{d}x)_{\text{exp}} $	$< 3 \sigma_{\text{TPC}}$
Primary track selections	DCA_z to PV	$< 2 \text{ cm}$
	DCA_r to PV	$< 7\sigma_r - 10\sigma_r (p_T)$
	number of SPD points	≥ 1
	number of TPC points	> 70
	χ^2 per cluster	< 4

Table 5: Track selections common to all decay daughters and primary track selections applied to the charged pions from decays of Ξ^{*0} .

327 Since pions and protons from weak decay of Λ ($c\tau = 7.89 \text{ cm}$ [10]) and pions from weak
 328 decay of Ξ^- ($c\tau = 4.91 \text{ cm}$ [10]) are produced away from the PV, specific topological and
 329 track selection criteria, as summarized in Table 6, were applied [11, 9, 12].

Topological cuts	p–Pb	Pb–Pb
DCA_r of Λ decay products to PV	$> 0.06 \text{ cm}$	$> 0.11 \text{ cm}$
DCA between Λ decay products	$< 1.4 \text{ cm}$	$< 0.95 \text{ cm}$
DCA of Λ to PV	$> 0.015 \text{ cm}$	> 0.06
$\cos\theta_\Lambda$	> 0.875	> 0.998
$r(\Lambda)$	$0.2 < r(\Lambda) < 100 \text{ cm}$	$0.2 < r(\Lambda) < 100 \text{ cm}$
$ M_{p\pi} - m_\Lambda $	$< 7 \text{ MeV}/c^2$	$< 7 \text{ MeV}/c^2$
DCA_r of pion (from Ξ^-) to PV	$> 0.015 \text{ cm}$	$> 0.035 \text{ cm}$
DCA between Ξ^- decay products	$< 1.9 \text{ cm}$	< 0.275
$\cos\theta_\Xi$	> 0.981	> 0.9992
$r(\Xi^-)$	$0.2 < r(\Xi^-) < 100 \text{ cm}$	$0.2 < r(\Xi^-) < 100 \text{ cm}$
$ M_{\Lambda\pi} - m_\Xi $	$< 7 \text{ MeV}/c^2$	$< 7 \text{ MeV}/c^2$

Table 6: Topological and track selection criteria.

331 In the analysis of Ξ^{*0} , Λ and π from Ξ^- were selected with a DCA of less than 1.9 cm
 332 and with a DCA_r to the PV greater than 0.015 cm. The Λ daughter particles (π and p)
 333 were required to have a DCA_r to the PV greater than 0.06 cm, while the DCA between the
 334 two particles was required to be less than 1.4 cm. Cuts on the invariant mass, the cosine

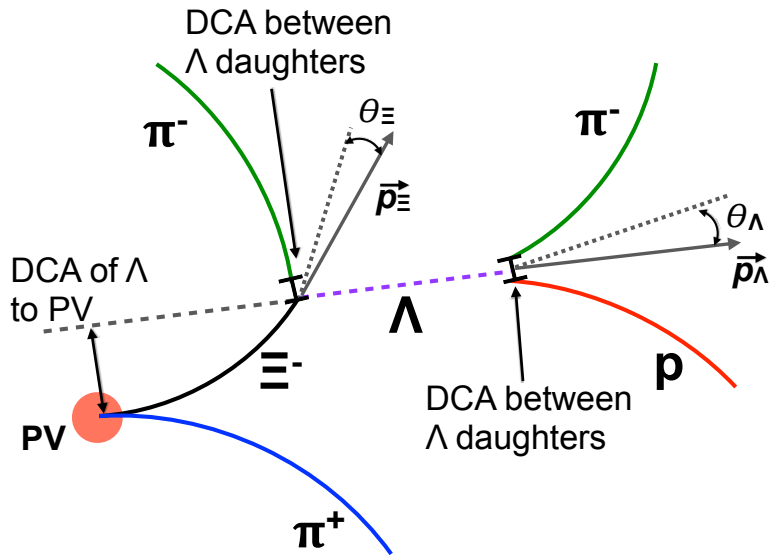


Figure 6: Sketch of the decay modes for Ξ^{*0} and depiction of the track and topological selection criteria.

³³⁵ of the pointing angle ($\theta_\Lambda, \theta_\Xi$) and the radius of the fiducial volume ($r(\Lambda), r(\Xi)$) in Table 6
³³⁶ were applied to optimize the balance of purity and efficiency of each particle sample.

337 **5.1.3 Particle identification**

338 PID selection criteria are applied for

- 339 1. π^\pm (last emitted π) and proton from Λ
340 2. π^\pm (second emitted π) from Ξ^\pm
341 3. π^\pm (first emitted π) from $\Xi(1530)^0$

342 by using TPC. On TPC dE/dx versus momentum distribution, 3σ cuts are applied to TPC
343 for selecting each of the particles. The TPC dE/dx selection allows to have better signal
344 with $\sim 20\%$ increase of significance.

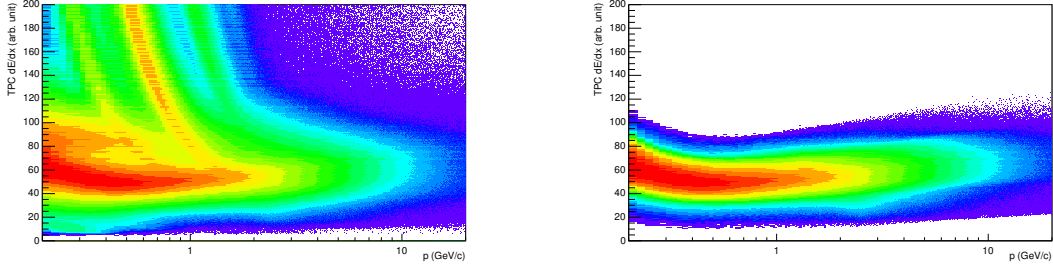


Figure 7: TPC dE/dx as function of transverse momentum for total (top) and selected first emitted π in 3σ (bottom)

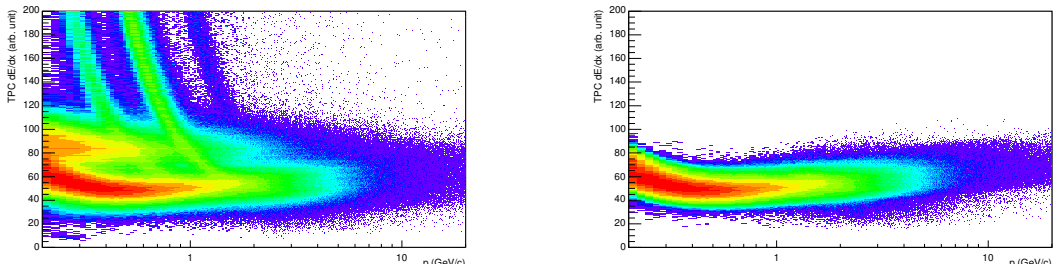


Figure 8: TPC dE/dx as function of transverse momentum for total (top) and selected second emitted π in 3σ (bottom)

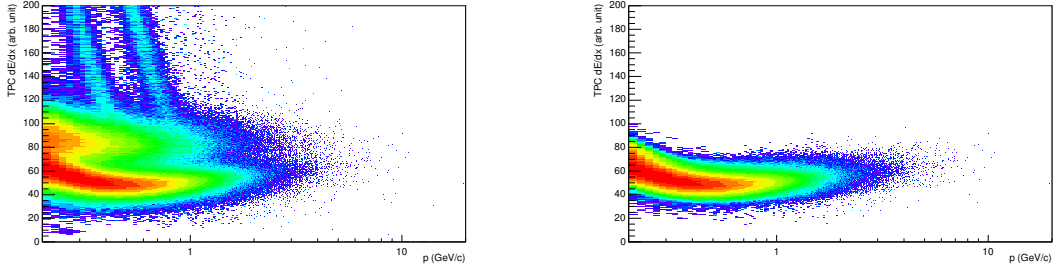


Figure 9: TPC dE/dx as function of transverse momentum for total (top) and selected last emitted π in 3σ (bottom)

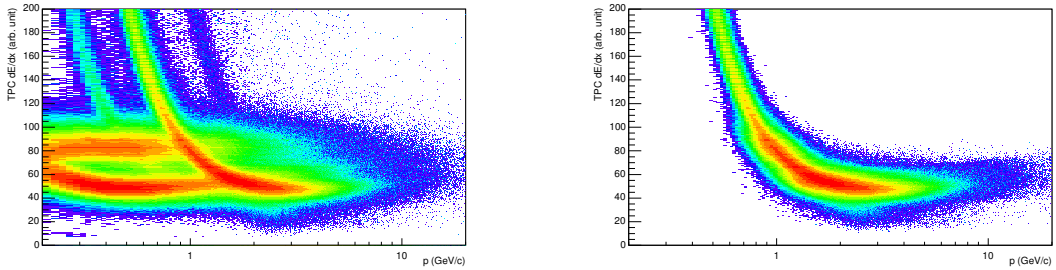


Figure 10: TPC dE/dx as function of transverse momentum for total (top) and selected proton in 3σ (bottom)

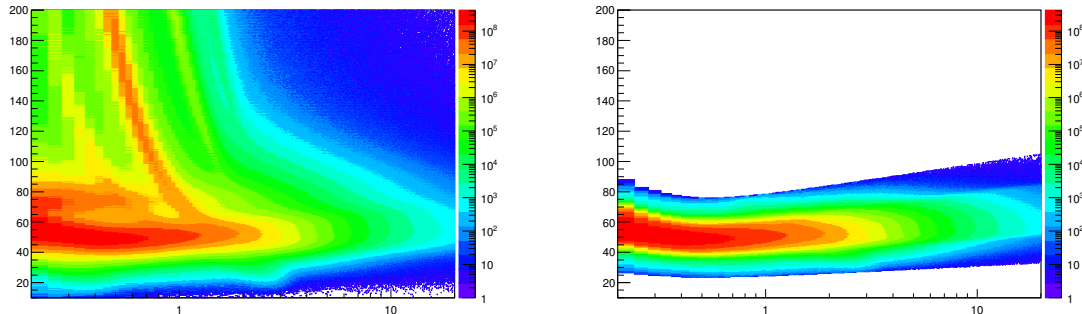


Figure 11: TPC dE/dx as function of transverse momentum for total (top) and selected first emitted π in 3σ (bottom)

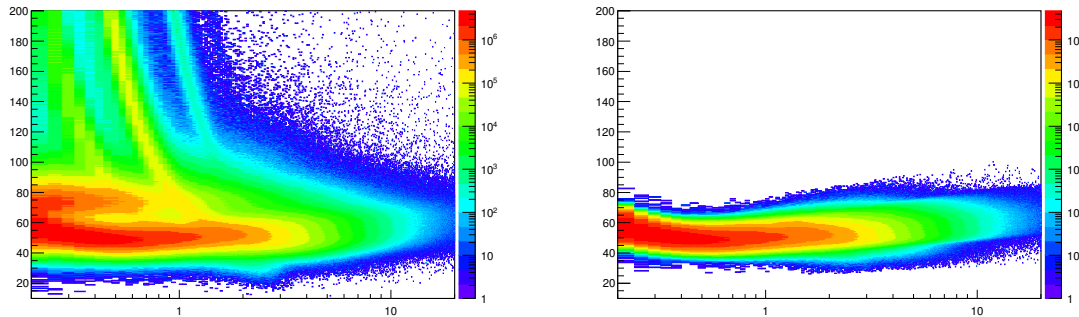


Figure 12: TPC dE/dx as function of transverse momentum for total (top) and selected second emitted π in 3σ (bottom)

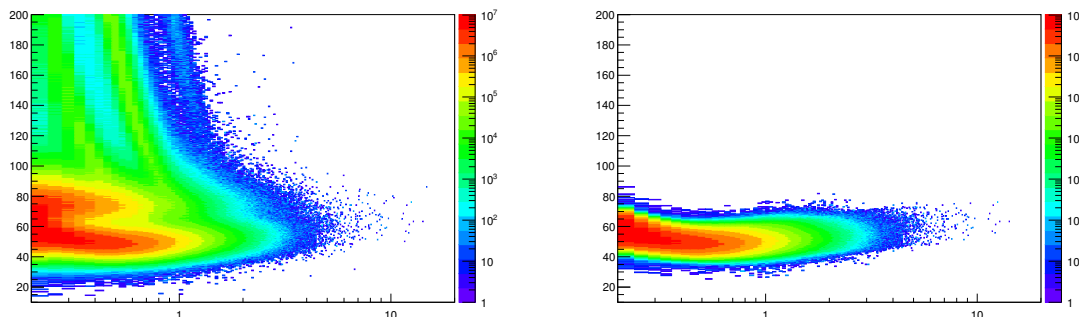


Figure 13: TPC dE/dx as function of transverse momentum for total (top) and selected last emitted π in 3σ (bottom)

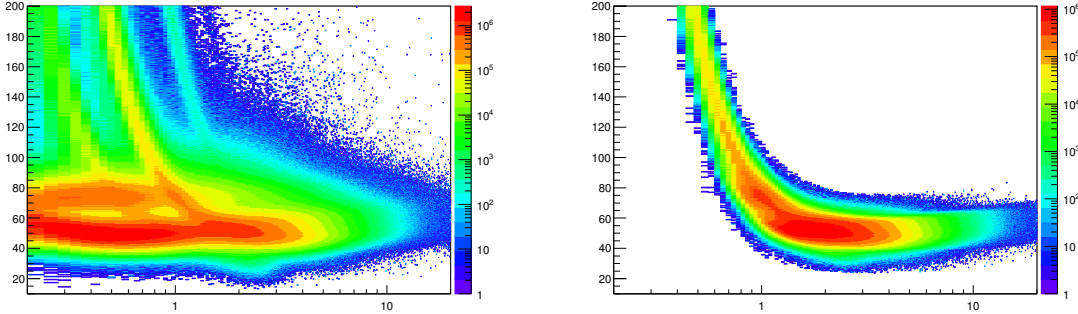


Figure 14: TPC dE/dx as function of transverse momentum for total (top) and selected proton in 3σ (bottom)

345 5.1.4 Signal extraction

346 The Ξ^{*0} signals were reconstructed by invariant-mass analysis of candidates for the decay
 347 products in each transverse momentum interval of the resonance particle, and for each
 348 multiplicity class. The $\Xi^-\pi^+(\Xi^+\pi^-)$ invariant mass distribution is reported in Figure 5.1.4
 349 for semi-central events (20-40%) in p-Pb collisions and Figure 5.1.4 for central events(0-
 350 10%) in Pb-Pb collisions.

351 Since the resonance decay products originate from a position which is indistinguishable
 352 from the PV, a significant combinatorial background is present. In order to extract
 353 $\Xi(1530)^0$ signal it is necessary to remove or, at least reduce, the combinatorial background.
 354 For this analysis, this has been done with the event mixing (EM) technique, by combining
 355 uncorrelated decay products 20 different events in p-Pb (5 different events in Pb-Pb). The
 356 events for the mixing have been selected by applying the similarity criteria to minimise
 357 distortions due to different acceptances and to ensure a similar event structure, only tracks
 358 from events with similar vertex positions z ($|\Delta z| < 1$ cm) and track multiplicities n ($|\Delta n| <$
 359 10) were taken.

360 The mixed-event background distributions were normalised to two fixed regions,
 361 $1.49 < M_{\Xi\pi} < 1.51 \text{ GeV}/c^2$ and $1.56 < M_{\Xi\pi} < 1.58 \text{ GeV}/c^2$, around the Ξ^{*0} mass
 362 peak (Figure 5.1.4 and 5.1.4). These regions were used for all p_T intervals and multiplicity
 363 classes, because the background shape is reasonably well reproduced in these regions and
 364 the invariant-mass resolution of the reconstructed peaks appears stable, independently of
 365 p_T . The uncertainty on the normalisation was estimated by varying the normalisation
 366 regions and is included in the quoted systematic uncertainty for the signal extraction (Section 5.4).

368 After the background subtraction, the resulting distribution is shown in Figure 5.1.4
 369 and 5.1.4. In order to obtain raw yields, a combined fit of a first-order polynomial for

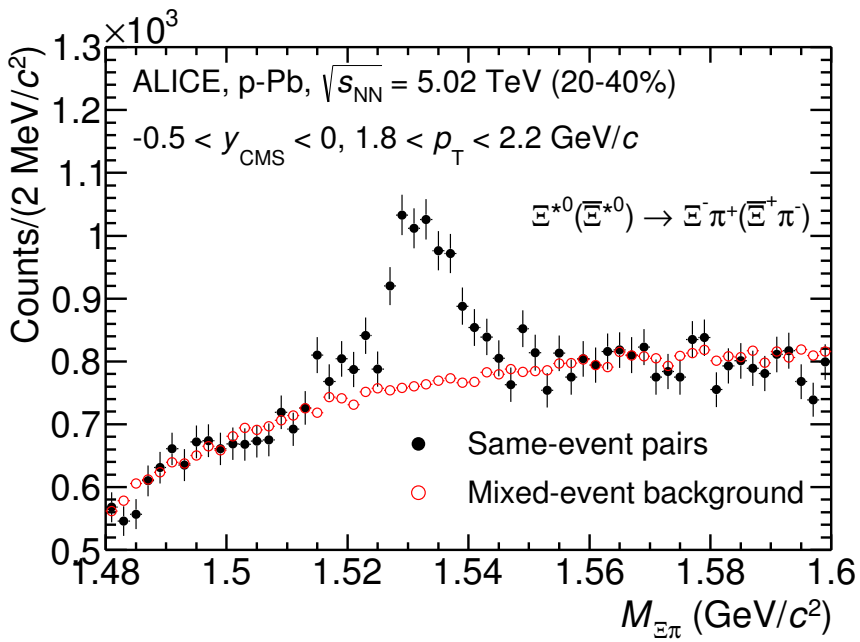


Figure 15: The $\Xi^\pm\pi^\pm$ invariant mass distribution (Same-event pairs) in $1.8 < p_T < 2.2 \text{ GeV}/c$ and for the multiplicity class 20-40%. The background shape, using pairs from different events (Mixed-event background), is normalised to the counts in $1.49 < M_{\Xi\pi} < 1.51 \text{ GeV}/c^2$ and $1.56 < M_{\Xi\pi} < 1.58 \text{ GeV}/c^2$.

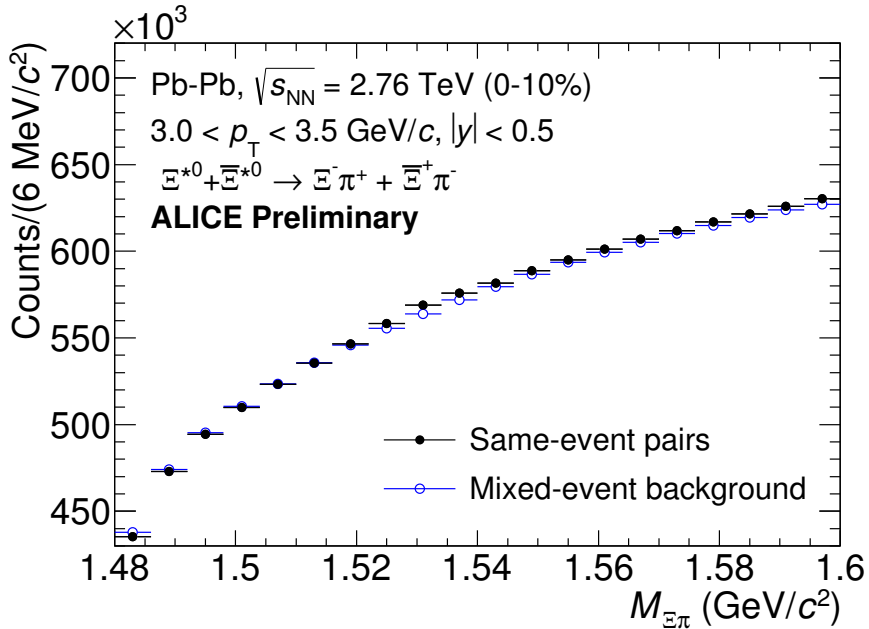


Figure 16: The $\Xi^\pm\pi^\pm$ invariant mass distribution (Same-event pairs) in $3.0 < p_T < 3.5$ GeV/c and for the centrality class 0-10%. The background shape, using pairs from different events (Mixed-event background), is normalised to the counts in $1.49 < M_{\Xi\pi} < 1.51$ GeV/c² and $1.56 < M_{\Xi\pi} < 1.58$ GeV/c².

370 the residual background and a Voigtian function (a convolution of a Breit-Wigner and a
 371 Gaussian function accounting for the detector resolution) for the signal was used. The
 372 mathematical form of fit function used in analysis is:

$$f(M_{\Xi\pi}) = \frac{Y}{2\pi} \frac{\Gamma_0}{(M_{\Xi\pi} - M_0)^2 + \frac{\Gamma_0^2}{4}} \frac{e^{-(M_{\Xi\pi} - M_0)/2\sigma^2}}{\sigma\sqrt{2\pi}} + bg(M_{\Xi\pi}) \quad (1)$$

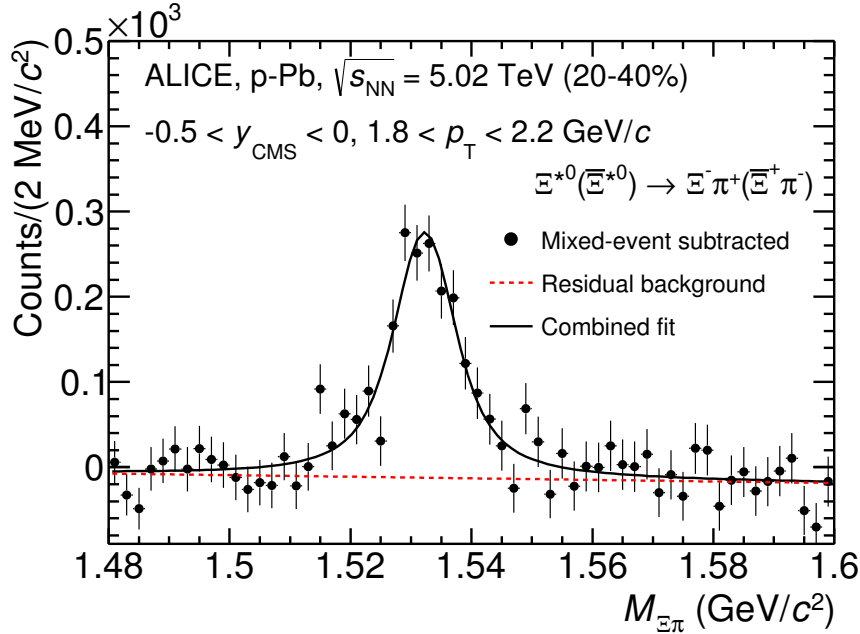


Figure 17: The invariant mass distribution after subtraction of the mixed-event background in p–Pb collisions. The solid curve represents the combined fit, while the dashed line describes the residual background.

373 The mass parameter of the Voigtian fit (M_0) is left free within the fit range ($1.48 \text{ GeV}/c^2$
 374 and $1.59 \text{ GeV}/c^2$). The overall invariant mass width of the Voigtian function is governed
 375 by 2 parameters: σ and Γ_0 . The σ describes the broadening of the peak due to finite
 376 detector resolution while Γ describes the intrinsic width of the resonance itself. The Γ_0 is
 377 fixed to the PDG value of $9.1 \text{ MeV}/c$ for the $\Xi(1530)^0$. Because of lack of statistics, the
 378 σ can be over estimated. Therefore the σ parameter is fixed to value derived from σ in
 379 MB events which has largest statistics. The σ as function of p_T distribution in MB events
 380 is shown in Figure. 19 and we also report invariant mass of $\Xi(1530)^0$ as function of p_T in
 381 Figure. 20. The $\Xi(1530)^0$ raw yields have been extracted from the fit for the 4 multiplicity

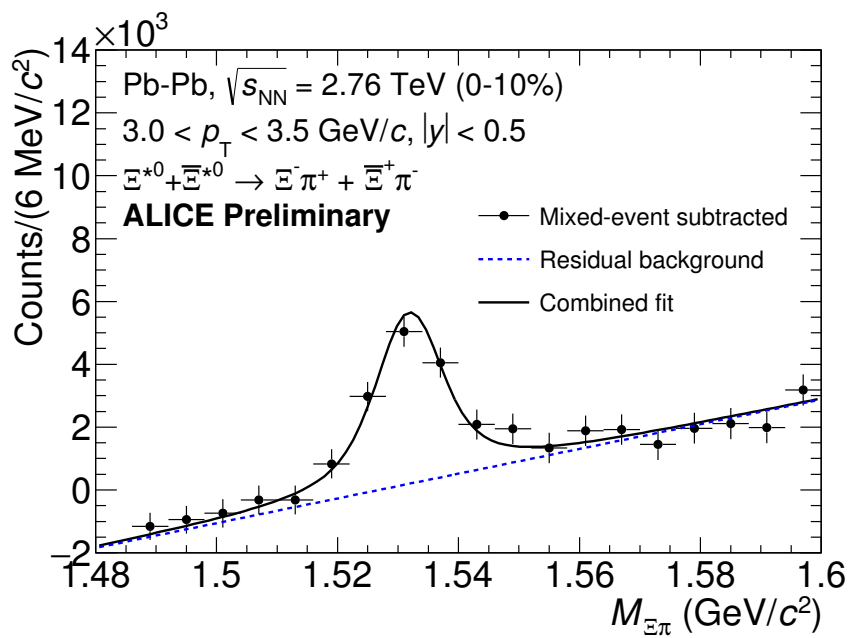


Figure 18: The invariant mass distribution after subtraction of the mixed-event background in Pb–Pb collisions. The solid curve represents the combined fit, while the dashed line describes the residual background.

³⁸² bins (+1NSD events) in p–Pb and 4 centrality bins in Pb–Pb collisions and the yields as
³⁸³ function of p_T are shown in Figure 21.

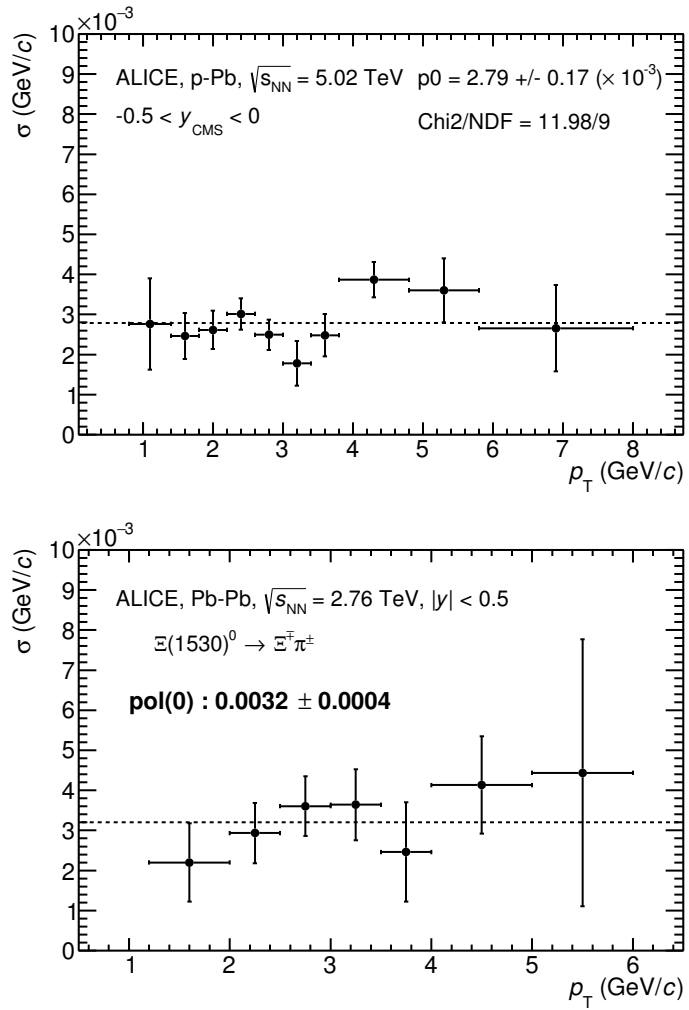


Figure 19: σ fit parameters as a function of p_T in MB in p–Pb collisions (top) and in Pb–Pb collisions (bottom).

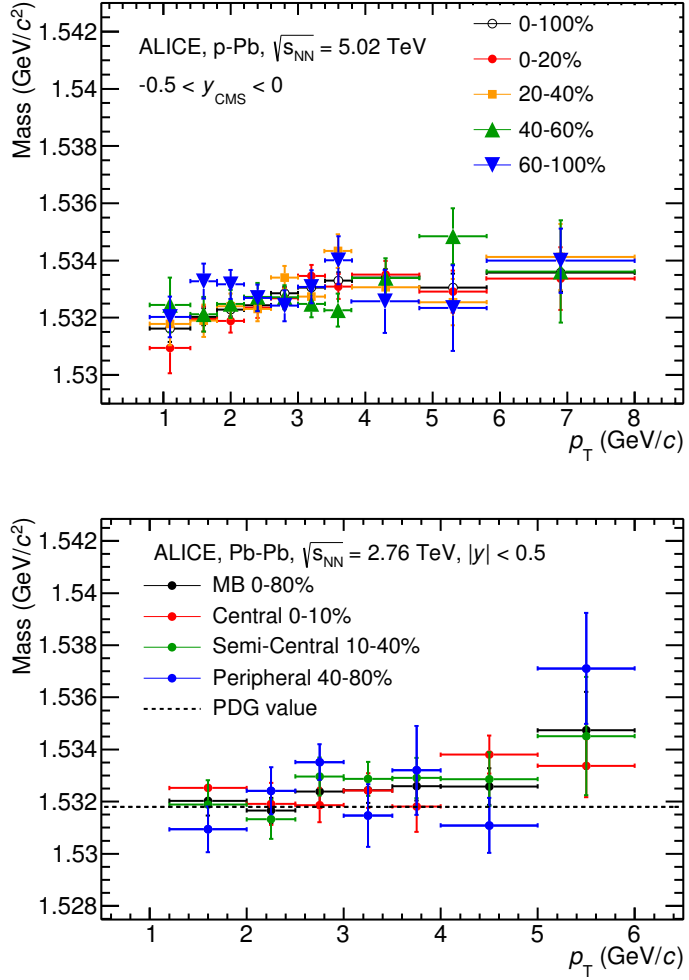


Figure 20: $\Xi(1530)^0$ -mass obtained from fit of the Voigtian peak as a function of p_T in each multiplicity classes in p-Pb collisions (top) and the different centrality classes in Pb-Pb (bottom).

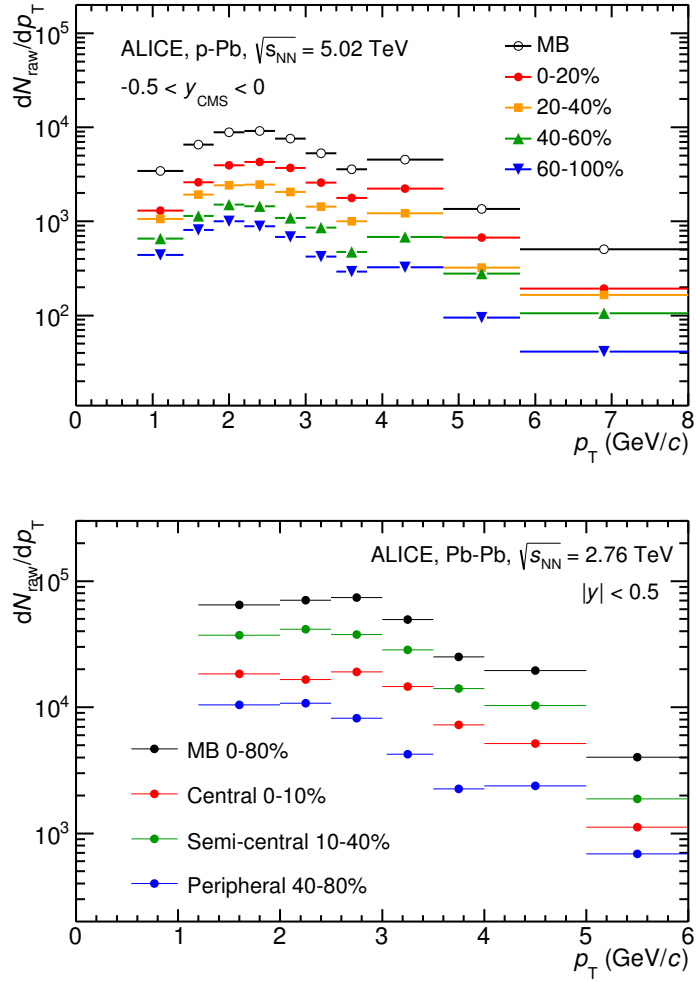


Figure 21: $\Xi(1530)^0$ -raw spectra obtained from fit of the Voigtian peak and a polynomial residual background for different multiplicities in p-Pb collisions (top) and Pb-Pb collisions (bottom). Only the statistical error is reported.

384 **5.2 Efficiency correction**

385 The raw yields were corrected for the geometrical acceptance and the reconstruction effi-
 386 ciency ($A \times \epsilon$) of the detector (Figure. 22). By using the DPMJET 3.05 event generator [13]
 387 and the GEANT 3.21 package [14], a sample of about 100 million p–Pb events was sim-
 388 ulated and reconstructed in order to compute the corrections. The distributions of $A \times \epsilon$
 389 were obtained from the ratio between the number of reconstructed Ξ^{*0} and the number of
 390 generated particle in the same p_T and rapidity interval. Since the correction factors for
 391 different multiplicity classes are in agreement with those from MB events within statistical
 392 uncertainty, the latter were used for all multiplicity classes.

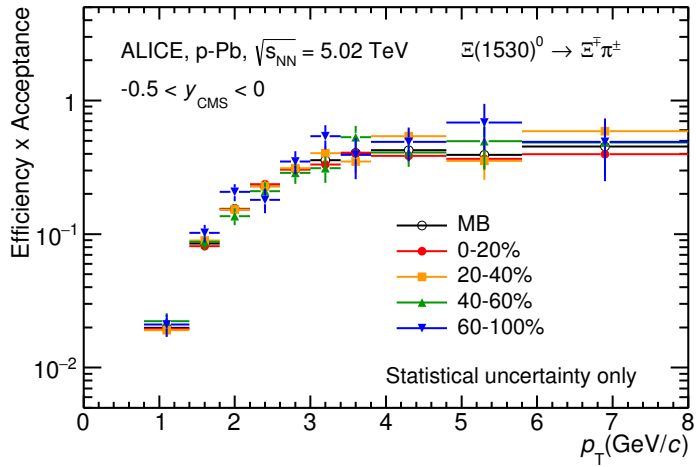


Figure 22: $\Xi(1530)^0$ -raw spectra obtained from fit of the Voigtian peak and a polynomial residual background for different multiplicities. Only the statistical error is reported.

393 Because the generated $\Xi(1530)^0$ spectra have different shapes than the measured $\Xi(1530)^0$
 394 spectra, it is necessary to weight the generated and reconstructed $\Xi(1530)^0$ spectra in these
 395 simulations. Fig. 23 shows the generated and reconstructed $\Xi(1530)^0$ spectra plotted with
 396 the (corrected) measured $\Xi(1530)^0$ spectrum for MB events and the Levy fit of that mea-
 397 sured spectrum. The generated and measured $\Xi(1530)^0$ spectra have different behaviours
 398 for the range $0.5 < p_T < 1$ GeV/ c . The generated $\Xi(1530)^0$ spectrum decreases with
 399 increasing p_T over this range, while the fit of the measured $\Xi(1530)^0$ spectrum reaches a
 400 local maximum in this range. The correction ϵ is observed to change rapidly over this
 401 p_T range. It is therefore necessary to weight the generated spectrum so that it has the
 402 shape of the measured $\Xi(1530)^0$ spectrum (and to apply corresponding weights to the re-
 403 constructed $\Xi(1530)^0$ spectrum). An iterative procedure is performed to determine the
 404 correct weighting (and therefore the correct ϵ).

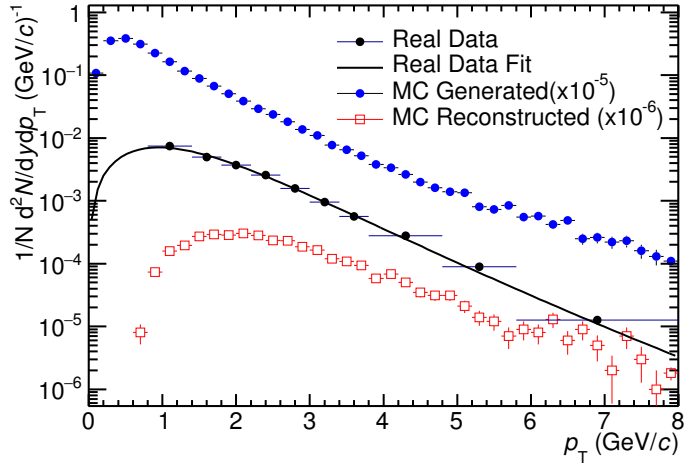


Figure 23: Real corrected $\Xi(1530)^0$ spectrum (black) for the minimum bias with Levy fit (black curve). Also shown are the unweighted generated (blue) and reconstructed (red) $\Xi(1530)^0$ spectra.

- 405 1. The unweighted ϵ is calculated.
- 406 2. This ϵ is used to correct the measured xis spectrum.
- 407 3. The corrected $\Xi(1530)^0$ spectrum is fit.
- 408 4. This fit is used to weight the simulated xis spectra. A p_T dependent weight is applied
409 to the generated xis spectrum so that it follows the fit. The same weight is applied
410 to the reconstructed xis spectrum.
- 411 5. The (weighted) ϵ is calculated.
- 412 6. Steps 2-5 are repeated (with the weighted ϵ from step 5 used as the input for step 2)
413 until the ϵ values are observed to change by $< 0.1\%$ (relative) between iterations. It
414 is observed that four iterations are sufficient for this procedure to converge.

415 Finally, the re-weighted efficiency is obtained and the distribution as function of p_T is
416 shown in Figure 24.

417 In order to obtain the correction factor dedicated in Pb-Pb collisions, MC events are
418 generated using Heavy Ion Jet Interaction Generator (HIJING). The generated events are
419 passed through a GEANT3 model of the ALICE experiment with a realistic description of
420 the detector response. Because we have observed centrality dependent efficiency, the cen-
421 trality dependent efficiencies have been applied to get corrected raw yield. The reweighting

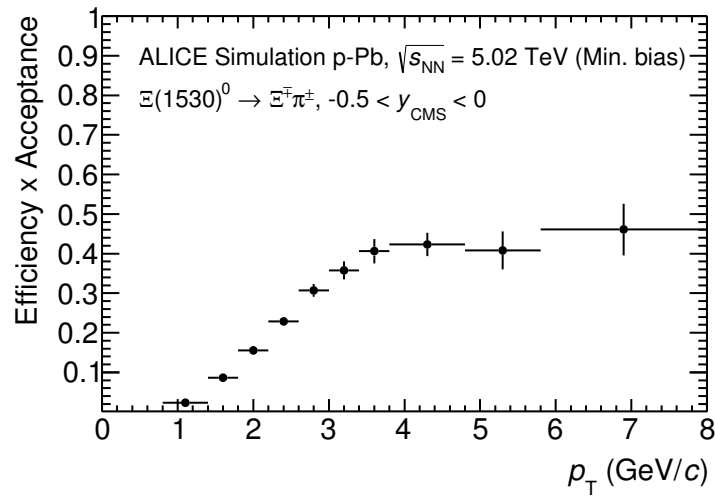


Figure 24: Efficiency as a function of p_T in minimum bias events in p–Pb collisions.

422 approach which was used to correct the efficiency in p–Pb is also applied to the efficiency
 423 obtained in Pb–Pb.

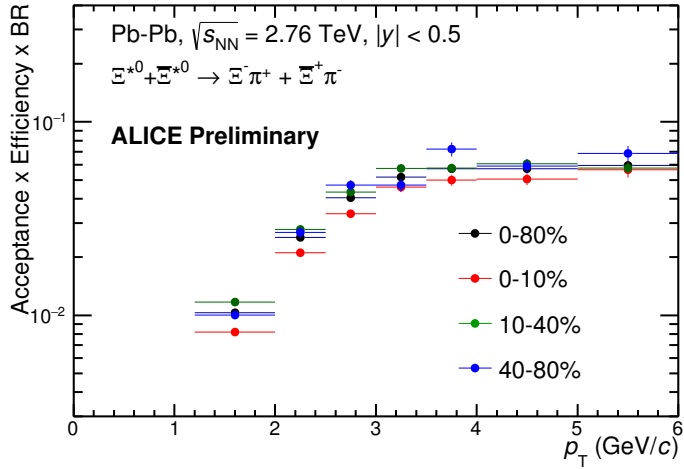


Figure 25: Efficiency as a function of p_T in different centrality classes in Pb–Pb collisions

424 5.3 Corrected p_T -spectra

425 The p_T spectrum is by the number of produced particles of a given type in the desired
 426 interval of phase-space divided by the number of inelastic collisions. The spectrum is
 427 calculated as:

$$\frac{1}{N} \times \frac{d^2N}{dydp_T} = \frac{1}{N_{E,PhysSel}} \times \frac{N_{raw}}{dp_T dy} \frac{1}{\epsilon} \frac{N_{total}^{MC}}{N_{post-PVcut}^{MC}}, \quad (2)$$

428 where N_E represent the number inelastic collisions, the $\frac{dN}{dydp_T}$ is the yield per range of
 429 rapidity y , per range in p_T . On the right hand side $N_{E,PhysSel}$ is the number of events
 430 counted by the physics selection trigger. N_{raw} is the raw extracted number of particle in the
 431 rapidity and p_T bin of width $\Delta y = 0.5$ in p–Pb ($\Delta y = 1.0$ in Pb–Pb) and Δp_T , respectively.
 432 ϵ is the reconstruction efficiency estimated from Monte Carlo simulations. $\frac{N_{total}^{MC}}{N_{post-PVcut}^{MC}}$ is the
 433 ratio of the total number of particle from MC divided by the number of particle from MC
 434 after the Primary-Vertex cut is imposed. It takes into account the fraction of particle lost
 435 after imposing the PV cut. We notice that for minimum-bias results in p–Pb, we adopted
 436 a normalisation such that to provide result from non-single diffractive(NSD) cross-section.
 437 The normalisation factor is 0.964 [6]. The obtained spectrum at MB and the spectrums
 438 from different multiplicity classes in p–Pb are shown in Figure 26 and different centrality
 439 classes in Pb–Pb are shown in Figure 27.

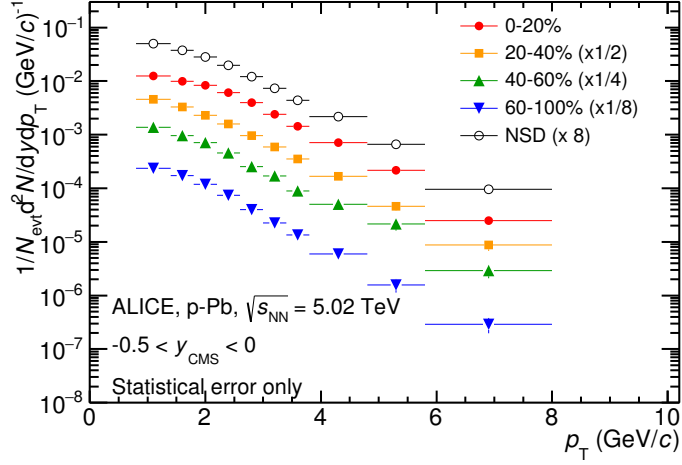


Figure 26: Corrected p_T -spectra of $\Xi(1530)^0$ in NSD and different multiplicity classes in p–Pb collisions.

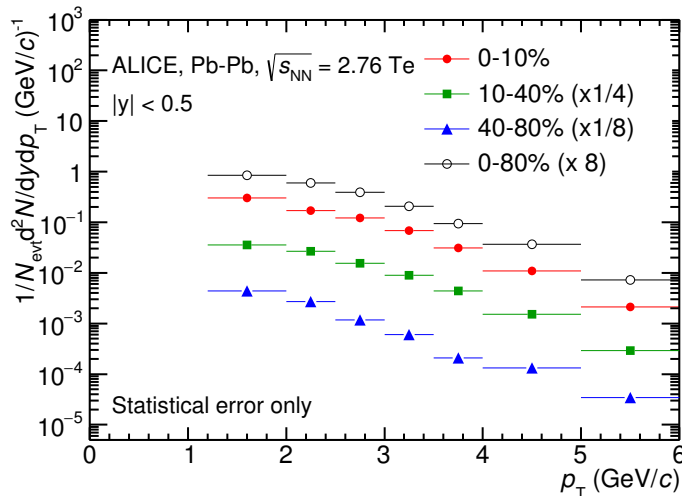


Figure 27: Corrected p_T -spectra of $\Xi(1530)^0$ in different centrality classes in Pb-Pb collisions.

440 **5.4 Systematic uncertainties**

441 The systematic uncertainties are calculated in seven principle groups. The procedure to ob-
 442 tain the systematic uncertainties is performed many times by varying the possible permuta-
 443 tion of the analysis parameter. The general strategy for evaluating systematic uncertainties
 444 is described as following:

- 445 1. Choose one set of parameters for the analysis as default
- 446 2. Observe the deviation of yield when one parameter is changed
- 447 3. The systematic uncertainty is calculated for a given source as the RMS deviation of
 448 the available sources.
- 449 4. The total systematic uncertainty, taking into account all the different sources, is the
 450 sum in quadrature of each source.

451 To study the systematic effect we repeat the measurement by varying one parameter at
 452 a time. A Barlow [15] check has been performed for each measurement to verify whether it
 453 is due to a systematic effect or a statistical fluctuation. Let each measurement be indicated
 454 by $(y_i \pm \sigma_i)$ and the central value (default measurement) by $(y_c \pm \sigma_c)$, one can define $\Delta\sigma_i$
 455 (Eq. 3).

$$\Delta\sigma_i = \sqrt{(|\sigma_i^2 - \sigma_c^2|)} \quad (3)$$

456 Then we calculate $n_i = \Delta y_i / \Delta\sigma_i$, where $\Delta y_i = |y_c - y_i|$. If $n_i \leq 1.0$ then the effects
 457 are due to the statistical fluctuation and if $n_i > 1.0$ we apply consistency check. Since
 458 the alternate and default measurements are not statistically independent, an alternate
 459 measurement which is statistically consistent with the default measurement should not be
 460 used in calculating a systematic uncertainty. The difference between the two measurements
 461 is $\Delta = y_c - y_i$. The difference in quadrature of the uncertainties is calculated by Eq. 3. It
 462 could be possible to check if $\Delta < \sigma$ and exclude such cases from the systematic uncertainties.
 463 However, there can be statistical fluctuations for which $\Delta > \sigma$. If the variations between the
 464 default and alternate measurements are purely statistical, the distribution of Δ/σ should
 465 be a Gaussian with a mean value that is consistent with zero and a deviation σ consistent
 466 with unity. In this analysis, if the mean value is less than 0.1 and σ is less than 1, the
 467 variation passes the consistency check.

468 Only the measurements which passed the Barlow check ($n_i > 1$) are used to determine
 469 the systematic uncertainty. For measurements $N > 2$, the systematic uncertainty has been
 470 determined as the RMS (eqn. 4) of the available measurements. If $N=2$, the absolute
 471 difference is assigned as systematic uncertainty.

$$\delta y_{syst.} = \sqrt{\frac{1}{N} \sum_i (y_i - \bar{y})^2} \quad (4)$$

472 Here N is the total number of available measurements including y_c and \bar{y} is the average
473 of value of the measurements. The measurement did not pass Barlow check, zero systematic
474 uncertainty has been assigned to the value.

475 By suing the way as explained above, all the main contributions to the systematic un-
476 certainty of particle spectra have been studied. In particular those that comes from signal
477 extraction, topological and kinematical selection cuts, track quality selection and $n\sigma$ TPC
478 PID variation. the meaning of each source of systematic uncertainty studied is described
479 in the following:

480

481 **Signal extraction**

482 We have extracted the signal with varying the yield calculating method which contains
483 the method of signal extraction by integrating the Voigtian fit function and bin counting.
484 We also have varied the normalisation range which is related to the invariant mass region
485 where the mixed events distribution is scaled to subtract the combinatorial background
486 and different background estimator such as Like-Sign distribution and polynomial fit was
487 taken account into the systematic source of signal extraction. The systematic uncertainty
488 from signal extraction is sum in quadrature of three sources.

489

490 **Topological selection**

491 To evaluate the stability of the chosen set of values for the topological cuts, loose and tight
492 cuts have beed defined in order to vary by $\pm 10\%$ respectively. The parameters are changed
493 once at a time. Total systematic uncertainty from topological selection is calculated by
494 summation in quadrature of nine sources.

495

496 **TPC $N_{cluster}$ selection**

497 The selection performed for the daughter tracks of the cascade is that $N_{cluster}$ is larger
498 than 70 and the value has been varied to 60 and 80 in order to estimate the systematic
499 uncertainty due to this selection.

500

501 **TPC dE/dx selection**

502 In order to evaluate any potential effect due to the TPC dE/dx selection (U_{PID}), the N_σ
503 selection was varied with $N = 2.5$ and 3.5 .

504

505 **p_T shape correction**

506 As described in Section 5.2, due to the different shape of the measured and generated
507 $\Xi(1530)^0$ spectra, we have applied reweighing procedure to the generated spectra to have
508 same shape and this correction is added into contributor of systematic uncertainty as
509 p_T shape correction.

510

511 **Mass window range selection**

512 In order to select Ξ^\pm which is daughter particle of $\Xi(1530)^0$, we apply the mass window

513 ± 7 MeV/ c^2 around $\Xi(1530)^0$ mass on $\Lambda\pi$ invariant mass distribution. The boundaries
514 has been varied to ± 6 MeV/ c^2 and ± 8 MeV/ c^2 to estimate systematic uncertainty.

515

516 **Vertex range selection**

517 The distribution of vertex-z is shown in Fig.3. The cut on |Vz| was varied from the nominal
518 ± 10 cm to ± 9 cm, ± 11 cm.

519

520 **Material Budget and hadronic cross section**

521 A possible source of uncertainty comes from the description of the material, active (de-
522 tecting area) or dead (structure and cable), that the particles cross during their travel in
523 the MC with respect to the real material present in the detector. Such description could
524 affect the reconstruction efficiency in different aspects (e.g. multiple scattering, energy
525 loss). The value estimated by Ξ analysis [16] has been used in this study which gives 4%
526 systematic uncertainty. In case of systematic uncertainty from hadronic cross section, we
527 have inherited the value studied in previous measurement[17] which amount is 1%.

528

529 **Tracking efficiency**

530 Systematic uncertainties from tracking efficiency from ITS + TPC combined track were
531 assigned as 3% in p–Pb and 4% in Pb–Pb collision system.[17]
532 (<https://twiki.cern.ch/twiki/bin/view/ALICE/TrackingEfficiencyCharged>)

533

534 Finally, total systematic uncertainty is sum in quadrature of sources listed above. Fig-
535 ure 28 and Figure 29 show the total systematic uncertainty in minimum bias event and
536 different multiplicity classes in p–Pb collisions, respectively. Again, Figure 30 and Figure
537 31 present the total systematic uncertainty in minimum bias event and different centrality
538 classes in Pb–Pb collisions.

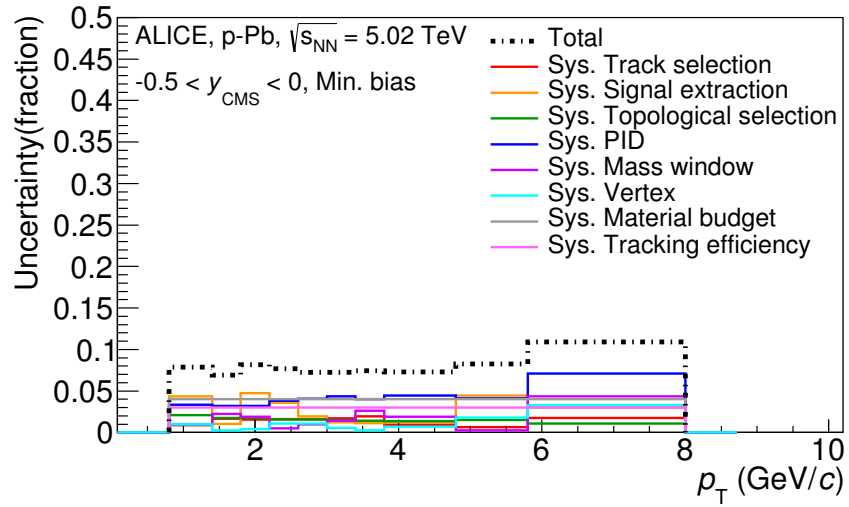


Figure 28: Summary of the contributions to the systematic uncertainty in minimum bias events in p–Pb collisions. The dashed black line is the sum in quadrature of all the contributions.

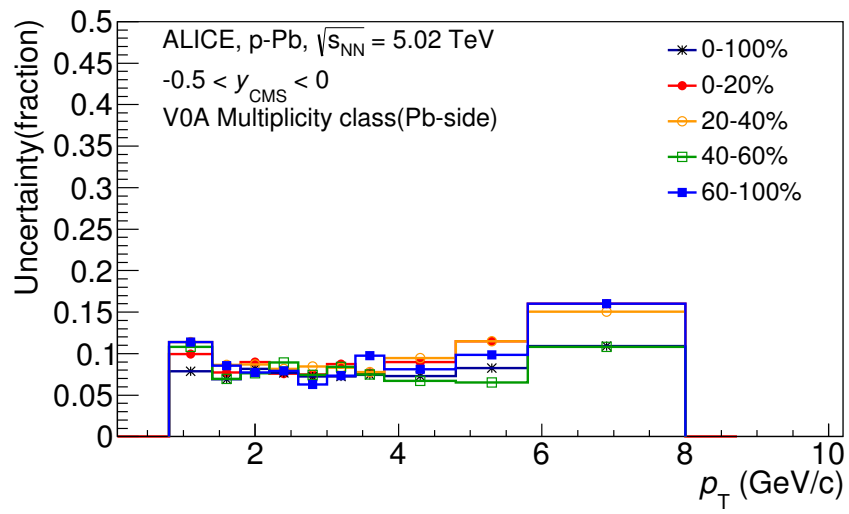


Figure 29: Systematic uncertainties for each multiplicity classes in p–Pb collisions.

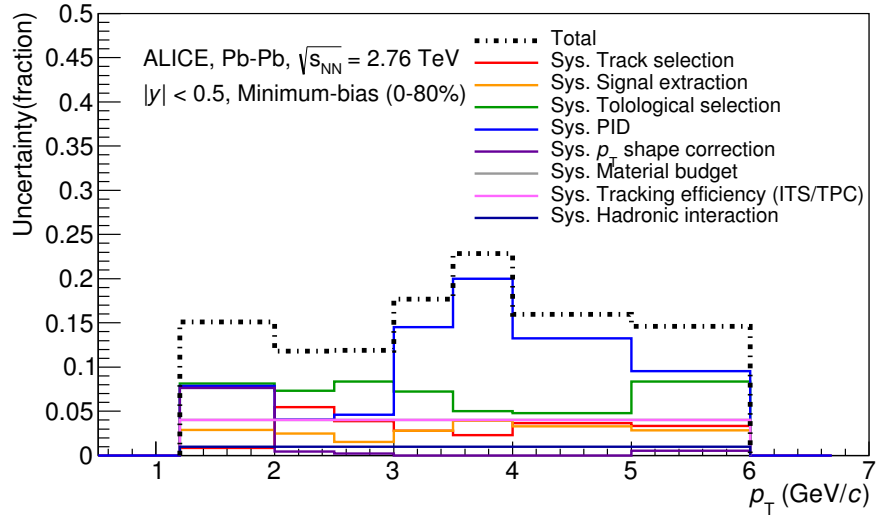


Figure 30: Summary of the contributions to the systematic uncertainty in minimum bias events in Pb–Pb collisions. The dashed black line is the sum in quadrature of all the contributions.

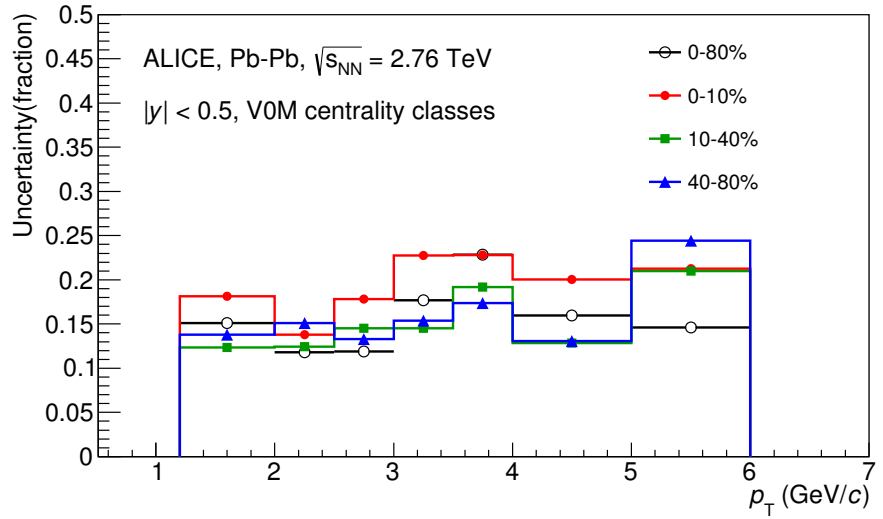


Figure 31: Systematic uncertainties for each multiplicity classes.

Source of uncertainty	$\Xi(1530)^0$ in p-Pb	$\Xi(1530)^0$ in Pb-Pb
<i>p_T-dependent</i>		
Tracking efficiency	3%	4%
Tracks selection	1-2%	1-5%
Topological selection	1-2%	5-8%
PID	3-7%	4-20%
Signal extraction	1-5%	1-4%
<i>p_T</i> shape correction	-	0-8%
Mass window (Ξ^{\pm})	4	-
Vertex selection	3%	-
<i>p_T-independent</i>		
Hadronic interaction	-	1%
Material budget	4%	4%
Branching ratio	0.3%	0.3%
Total	8-12%	9-25 %

Table 7: Summary of the systematic uncertainties on the differential yield, $d^2N/(dp_T dy)$. Minimum and maximum values in all p_T intervals and multiplicity classes in p–Pb, centrality classes in Pb–Pb are shown for each source.

539 **5.5 $\Xi(1530)^0$ transverse momentum spectra**

540 The raw yield shown in Figure 26 and 27 have been corrected for efficiency as described
 541 in section 5.2. The measured spectra for $(\Xi(1530)^0 + \bar{\Xi}(1530)^0)/2$ are reported in Figure
 542 32 for p–Pb collisions and Figure 33 for Pb–Pb collisions. The statistical and systematic
 543 uncertainties are reported respectively as the error bars and the boxes on the plot. The
 544 corrected yields for p–Pb collisions are measured with $0.8 < p_T < 8.0$ GeV/c while the
 545 yields for Pb–Pb collisions are obtained with $1.2 < p_T < 6.0$ GeV/c due to difficulty of
 546 signal extraction in low and high p_T region.

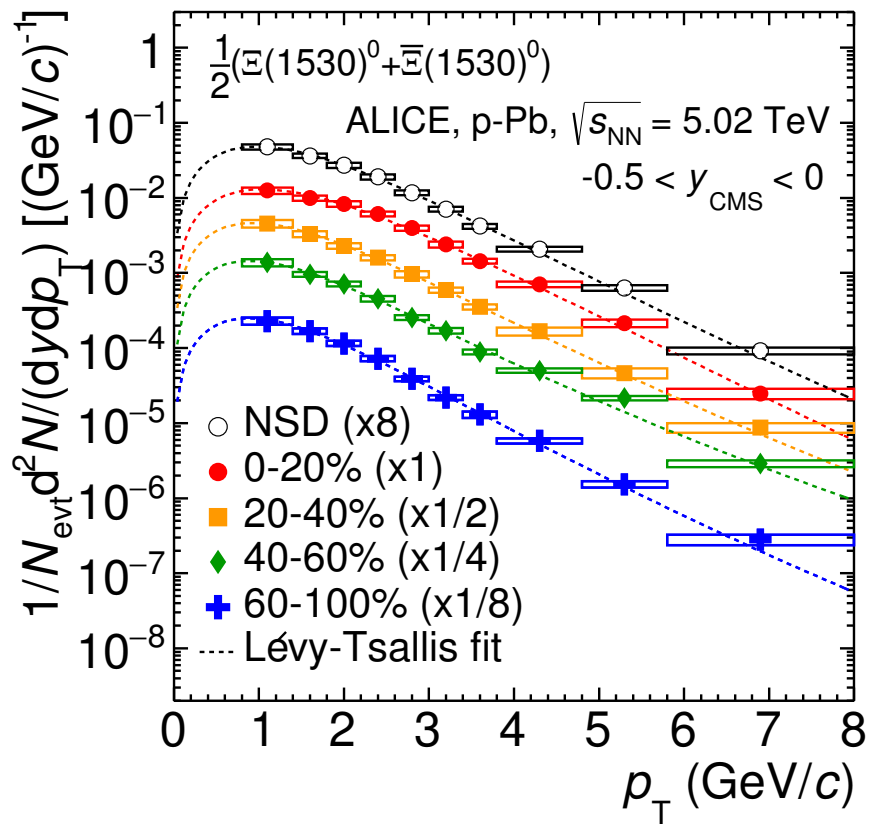


Figure 32: Corrected yields as function of p_T in NSD events and multiplicity dependent event classes in p-Pb collision system. Statistical uncertainties are presented as bar and systematical uncertainties are plotted as boxes.

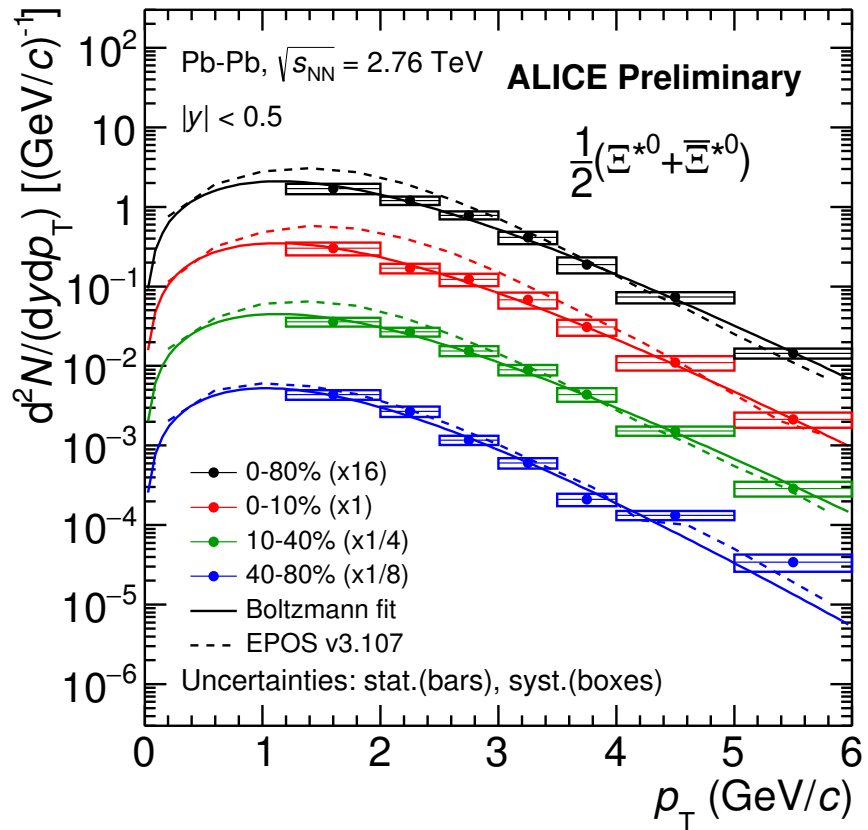


Figure 33: Corrected yields as function of p_T in different centrality classes in Pb-Pb collision system. Statistical uncertainties are presented as bar and systematical uncertainties are plotted as boxes.

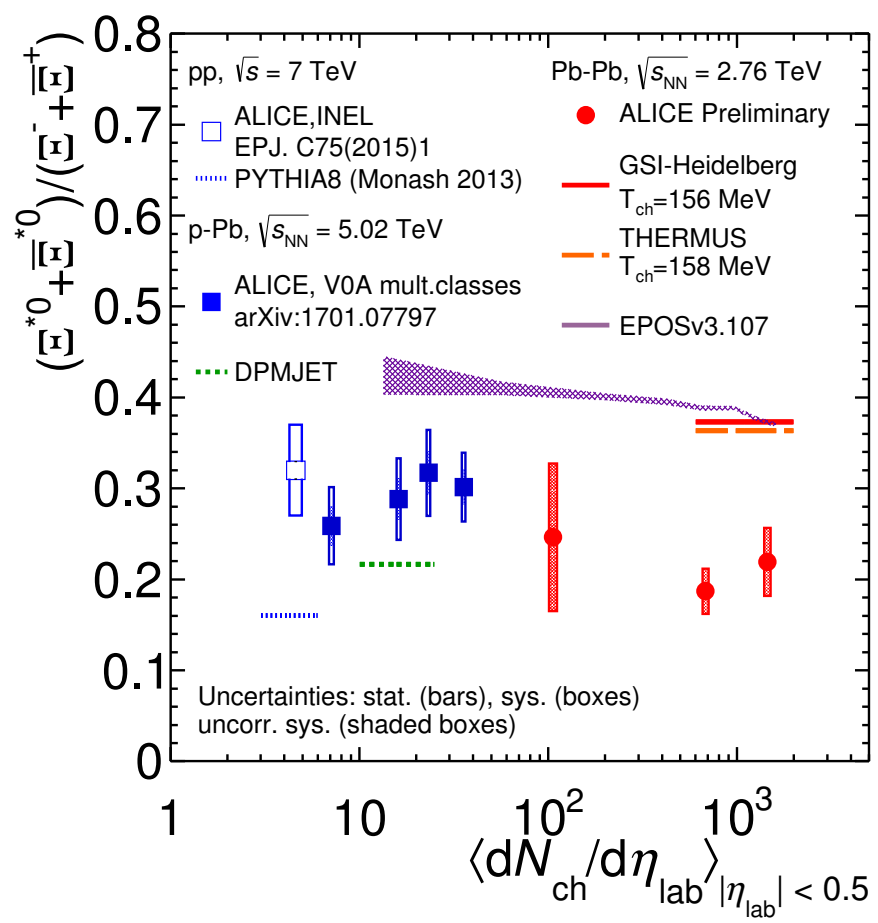


Figure 34: Integrated.

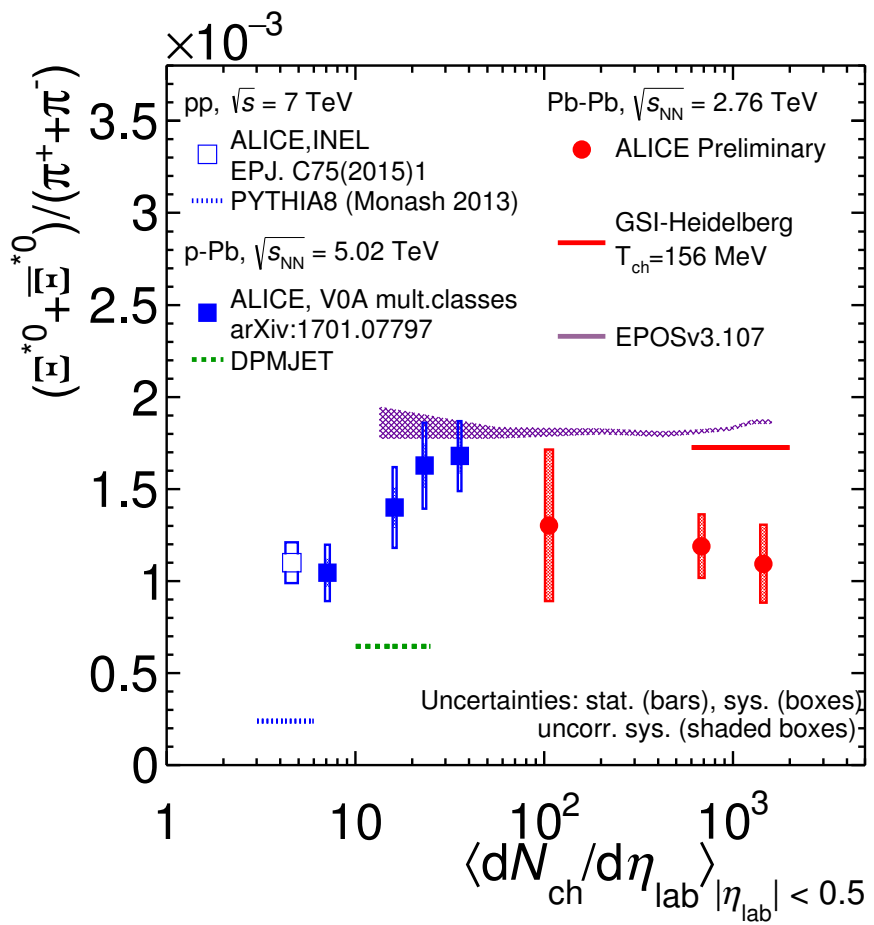


Figure 35: Integrated.

547 **6 Results**

548 **6.1 dN/dy and $\langle p_T \rangle$**

549 **6.2 Particle yield ratios**

550 **6.2.1 Comparison with other resonances**

551 **6.2.2 Comparison with models**

552 **References**

- 553 [1] D. Hahn and H. Stoecker, “THE QUANTUM STATISTICAL MODEL OF
554 FRAGMENT FORMATION: ENTROPY AND TEMPERATURE EXTRACTION
555 IN HEAVY ION COLLISIONS,” *Nucl. Phys.* **A476** (1988) 718–772.
- 556 [2] S. Wheaton, J. Cleymans, and M. Hauer, “THERMUS: A Thermal model package
557 for ROOT,” *Comput. Phys. Commun.* **180** (2009) 84–106, [hep-ph/0407174](#).
- 558 [3] J. Cleymans, S. Kabana, I. Kraus, H. Oeschler, K. Redlich, and N. Sharma,
559 “Antimatter production in proton-proton and heavy-ion collisions at ultrarelativistic
560 energies,” *Phys. Rev.* **C84** (2011) 054916, [arXiv:1105.3719 \[hep-ph\]](#).
- 561 [4] **ALICE** Collaboration, K. Aamodt *et al.*, “The ALICE experiment at the CERN
562 LHC,” *JINST* **3** (2008) S08002.
- 563 [5] **ALICE** Collaboration, B. Abelev *et al.*, “Performance of the ALICE Experiment at
564 the CERN LHC,” *Int. J. Mod. Phys.* **A29** (2014) 1430044, [arXiv:1402.4476](#)
565 [[nucl-ex](#)].
- 566 [6] **ALICE** Collaboration, J. Adam *et al.*, “Production of $K^*(892)^0$ and $\phi(1020)$ in
567 $p\text{-Pb}$ collisions at $\sqrt{s_{NN}} = 5.02$ TeV,” *Eur. Phys. J.* **C76** (2016) 245,
568 [arXiv:1601.7868 \[nucl-ex\]](#).
- 569 [7] **ALICE** Collaboration, B. Abelev *et al.*, “Pseudorapidity Density of Charged
570 Particles in $p\text{-Pb}$ Collisions at $\sqrt{s_{NN}} = 5.02$ TeV,” *Phys. Rev. Lett.* **110** (2013)
571 032301, [arXiv:1210.3615 \[nucl-ex\]](#).
- 572 [8] **ALICE** Collaboration, B. Abelev *et al.*, “Centrality determination of Pb–Pb
573 collisions at $\sqrt{s_{NN}} = 2.76$ TeV with ALICE,” *Phys. Rev.* **C88** (2013) ,
574 [arXiv:1303.0737 \[nucl-ex\]](#).
- 575 [9] **ALICE** Collaboration, B. Abelev *et al.*, “Production of $\Sigma(1385)^{\pm}$ and $\Xi(1530)^0$ in
576 proton-proton collisions at $\sqrt{s} = 7$ TeV,” *Eur. Phys. J.* **C75** (2015) 1,
577 [arXiv:1406.3206 \[nucl-ex\]](#).

- 578 [10] **Particle Data Group** Collaboration, K. Olive *et al.*, “Review of Particle Physics,”
579 *Chin. Phys. C***38** (2014) 090001.
- 580 [11] **ALICE** Collaboration, J. Adam *et al.*, “Multi-strange baryon production in p–Pb
581 collisions at $\sqrt{s_{\text{NN}}}=5.02$ TeV,” *Phys. Lett. B***758** (2016) 389–401,
582 [arXiv:1512.07227 \[nucl-ex\]](https://arxiv.org/abs/1512.07227).
- 583 [12] **ALICE** Collaboration, K. Aamodt *et al.*, “Strange particle production in
584 proton-proton collisions at $\sqrt{s}=0.9$ TeV with ALICE at the LHC,” *Eur. Phys. J.*
585 **C71** (2011) 1594, [arXiv:1012.3257 \[nucl-ex\]](https://arxiv.org/abs/1012.3257).
- 586 [13] S. Roesler, R. Engel, , and J. Ranft, “The Monte Carlo Event Generator
587 DPMJET-III, Advanced Monte Carlo for Radiation Physics, Particle Transport
588 Simulation and Applications,” *Conference Proceedings, MC2000, Lisbon, Portugal,*
589 *October 23–26* (2000) 1033–1038, [hep-ph/0012252](https://arxiv.org/abs/hep-ph/0012252).
- 590 [14] R. Brun, F. Carminati, and S. Giani, “GEANT detector description and simulation
591 tool,” *CERN-W5013* (1994) .
- 592 [15] R. Barlow, “Systematic Errors: Facts and Fictions,” *Presented at Advanced*
593 *Statistical Techniques in HEP, Durham, March 2002* (2002) 333p,
594 [hep-ex/0207026v1](https://arxiv.org/abs/hep-ex/0207026v1).
- 595 [16] **ALICE** Collaboration, B. Abelev *et al.*, “Multi-strange baryon production at
596 mid-rapidity in Pb–Pb collisions at $\sqrt{s_{\text{NN}}}=2.76$ TeV,” *Phys. Lett. B***728** (2014)
597 216–227, [arXiv:1307.5543 \[nucl-ex\]](https://arxiv.org/abs/1307.5543).
- 598 [17] **ALICE** Collaboration, B. Abelev *et al.*, “Centrality dependence of π , K and p
599 production in Pb–Pb collisions at $\sqrt{s_{\text{NN}}}=2.76$ TeV,” *Phys. Rev. C***88** (2013) ,
600 [arXiv:1301.4361 \[nucl-ex\]](https://arxiv.org/abs/1301.4361).

601 **Acknowledgements**